# A Cryptic Interfacial Pocket Uncovered in Full CRL4$^{CRBN}$–IKZF3 Ubiquitylation Complex Enhances IMiD Efficacy

Zhiheng Deng[1]†, Huasong Ai[2]†*, Qiang Shi[1]†, Jiawei Liang[1], Zaozhen He[1], Jiqing Zheng[1], Haoxiang Li[1], Liying Zhang[1], Wei He[1], Shixian Tao[1], Qingyun Zheng[2], Wei He[3], Man Pan[2]*, Lei Liu[1]*

**Affiliations:**

[1]New Cornerstone Science Laboratory, Tsinghua-Peking Joint Center for Life Sciences, Ministry of Education Key Laboratory of Bioorganic Phosphorus Chemistry and Chemical Biology, Center for Synthetic and Systems Biology, Department of Chemistry, Tsinghua University, Beijing, China.

[2]Institute of Translational Medicine, School of Pharmaceutical Sciences, School of Chemistry and Chemical Engineering, National Center for Translational Medicine (Shanghai), Shanghai Key Laboratory for Antibody-Drug Conjugates with Innovative Target, Shanghai Jiao Tong University, Shanghai, China.

[3]School of Pharmaceutical Sciences, Tsinghua University, Beijing, China.

*Corresponding author. Email: huasongai@sjtu.edu.cn (H.A.); panman@sjtu.edu.cn (M.P.); lliu@mail.tsinghua.edu.cn (L.L.)

†These authors contributed equally to this work.

**Abstract:** Immunomodulatory imide drugs (IMiDs) redirect the CUL4–RBX1–DDB1–CRBN (CRL4$^{CRBN}$) ligase to ubiquitylate and degrade disease-linked proteins, but the full picture of how IMiDs glue the neosubstrate within the whole CRL4$^{CRBN}$ complex remains unknown. We determined cryo-electron microscopy structures of eight approved or clinical IMiDs in full CRL4$^{CRBN}$ ubiquitylation complexes at resolutions up to 3.4 Å, and revealed how these structurally distinct IMiDs exploit the structural plasticity of CRL4$^{CRBN}$ to organize conformationally conserved and compact active ubiquitylation assemblies with the neosubstrate IKZF3. Four "next-generation" IMiDs were found to additionally engage a cryptic gluing-driven interfacial (GDI) pocket at the non-degron zinc finger 3 (ZF3) of IKZF3, which contributes to their enhanced efficacy and neosubstrate specificity. The identification of cryptic gluing-driven pockets formed only in full ubiquitylation complexes provides new structure-directed design opportunities for IMiDs to improve therapeutic efficacy.

## Introduction

Transcending its tragic clinical origins, the teratogenic drug thalidomide (*1*) was discovered to be repurposable for treating diseases with historically limited therapeutic options, particularly in oncology and hematology (*2*). This fortuitous finding has both paralleled and driven myriad innovations in the history of pharmaceuticals. Thalidomide-inspired immunomodulatory imide drugs (IMiDs), including lenalidomide and pomalidomide, function through cereblon (CRBN) as part of the $CRL4^{CRBN}$ E3 ligase complex (*3-5*) and have demonstrated remarkable clinical efficacy in treating multiple myeloma (*6*). IMiDs recruit the $CRL4^{CRBN}$ E3 ligase complex to ubiquitylate and facilitate the subsequent degradation of specific cellular substrates, including the Ikaros family transcription factors, IKZF1 and IKZF3 (*7-9*), and casein kinase 1α (CK1α) (*10*), leading to tumor suppression and immune modulation. These agents demonstrate high efficacy, with lenalidomide generating over $12 billion in annual sales and pomalidomide showing improved survival in relapsed/refractory patients (*6, 11*).

Decades of studies have elucidated how IMiDs rewire protein–protein interactions (PPIs) to achieve therapeutic consequences (*12-15*). A plethora of structural work focused on the static IMiD–CRBN binary complex and neosubstrate–IMiD–CRBN ternary complex has revealed that IMiDs directly bind to the CRBN thalidomide-binding domain (TBD) and create a neo-interface to engage substrate degrons, such as the G-loop motif, to enable subsequent ubiquitylation and degradation of the target protein (*16-33*). Recent advances have further revealed dynamic allostery: IMiDs trigger CRBN conformational changes from an “open” to a “closed” state, facilitating the binding of Ikaros transcription factors (*24*). Although these studies have advanced our understanding of how IMiDs glue the neosubstrate and CRBN (*12-15*), the complete molecular picture of how IMiDs glue the neosubstrate to induce ubiquitylation within the intact, catalytically active $CRL4^{CRBN}$ ligase complex remains unknown, which is of particular importance in the context that the optimization of IMiD pharmacology based on the ternary complex models does not fully correlate with therapeutic efficacy (*19, 34*).

Here, we present cryo-electron microscopy (cryo-EM) structures of eight approved and clinical IKZF3-targeting IMiDs in complex with the neosubstrate IKZF3 and fully Nedd8-activated $CRL4^{CRBN}$ ($_{N8}CRL4^{CRBN}$) ligase and provide the first comprehensive molecular portrait of how IMiDs engage the intact, catalytically active $CRL4^{CRBN}$ ubiquitylation machinery to induce neosubstrate ubiquitylation. We unexpectedly observed that “next-generation” IMiDs, such as mezigdomide and golcadomide, can additionally bind to the non-degron zinc finger 3 (ZF3) of IKZF3 via an unprecedented cryptic gluing-driven interfacial (GDI) pocket, mediating additional drug–protein interactions and enhancing IKZF3 ubiquitylation and degradation efficiency. Thus, the full molecular portrait of IMiD-induced neosubstrate ubiquitylation offers more

comprehensive and functionally relevant mechanistic insights into the efficacy of IMiDs than binary or ternary complexes do, informing a structure-guided design strategy targeting the GDI pocket to improve therapeutic efficacy.

## Approved and clinical IMiDs induce IKZF3 ubiquitylation and mediate IKZF3 degradation with varying efficiencies

Currently, eight approved or clinical IMiDs with known chemical structures have been reported to degrade IKZF3 (fig. S1A): thalidomide (*7*), lenalidomide (CC-5013) (*7-9*), pomalidomide (CC-4047) (*7-9*), avadomide (CC-122) (*10, 35*), iberdomide (CC-220) (*29, 36*), mezigdomide (CC-92480) (*37*), golcadomide (CC-99282) (*38, 39*), and cemsidomide (CFT7455) (*40*). Prior proteomic profiling of MM1S multiple myeloma cells identified lysine 166 (K166) as the top-ranking IMiD-regulated ubiquitylation site located within the zinc finger 2 (ZF2) degron motif of IKZF3 (*7*). In our experiments, we first verified the potency of these eight IMiDs to induce IKZF3 degradation in cells (figs. S1B, S1C), providing a relative ranking of the IKZF3 degradation-inducing potency of these eight IMiDs: thalidomide and lenalidomide exhibited weaker potency; pomalidomide and avadomide showed enhanced potency; and iberdomide, mezigdomide, golcadomide, and cemsidomide demonstrated strong IKZF3 degradation-inducing potency (figs. S1B, S1C). Next, we conducted mass spectrometry analysis of IKZF3 ubiquitylated *in vitro* in the presence of IMiDs (figs. S1D, S1E). Three IKZF3 lysine residues (K158, K166, and K172) modified with the GG remnant were consistently identified in eight IMiD-induced ubiquitylation reactions (fig. S1D). Among them, K166 had the highest number of peptide-spectrum matches (PSMs), confirming that it is the most extensively ubiquitylated lysine (fig. S1D). Taken together, these data show that eight IMiDs can induce IKZF3 degradation with varying efficiencies and that the lysine residue K166 of IKZF3 is the preferential ubiquitylation site.

## Cryo-EM structures unveil a unified conformation of eight $_{N8}CRL4^{CRBN}$–IMiD–IKZF3 active ubiquitylation assemblies

Next, we aimed to determine the cryo-EM structures of a fully assembled active $_{N8}CRL4^{CRBN}$ ligase with the UbcH5a~Ub thioester ('~' represents an activated thioester bond between the donor ubiquitin and the E2 catalytic cysteine), positioned at the catalytic apex for ubiquitin transfer to IKZF3 K166 in the presence of eight discrete IMiDs. Since the IMiD-induced substrate ubiquitylation transition state is fleeting (fig. S2A), an activity-based chemical trapping strategy (*41-43*) was employed to engineer covalent connectivity between the donor ubiquitin carboxyl terminus and the IKZF3 K166 site (figs. S2B–S2D) and crosslink to the UbcH5a catalytic cysteine, facilitating the formation of a stable topological mimic of the native ubiquitylation transition state

(fig. S2A). Eight complexes were reconstituted in the presence of individual IMiD molecules and purified via size-exclusion chromatography (SEC, fig. S2E and 2F). Single-particle cryo-EM analysis yielded high-quality maps of eight $_{N8}$CRL4$^{CRBN}$–IMiD–IKZF3 ubiquitylation assemblies, which were refined to an overall resolution of 3.4–3.8 Å (Figs. 1A and 1B, fig S3, table S1 and S2, and data S1). The ubiquitylation assembly adopted a large, closed, carabiner-like conformation (180 Å by 120 Å, Fig. 1B), with all expected individual components clearly observed and unambiguously modeled (Figs. 1B and 1C, fig. S4), including the IMiD molecules (Figs. 1B, 1C).

The intact ubiquitylation assembly was structurally divided into three functional modules: the ternary module, the cullin scaffold, and the catalytic module (Fig. 1D). The ternary module consists of the substrate adaptor DDB1, the substrate receptor CRBN, the target protein IKZF3, and the IMiD molecule sandwiched by CRBN and IKZF3. The intermedial helical bundle (HB) of CRBN is embraced by two DDB1 β-propeller folds, BPA and BPC (Fig. 1D). The phthalimide/glutarimide cores of eight individual IMiDs are deeply buried in the CRBN thalidomide-binding domain (TBD) pocket, creating a neo-interface for engaging the G-loop of the IKZF3 ZF2 motif (fig. S5A). In the cullin scaffold, CUL4A adopts an arc-shaped conformation, with its activator Nedd8 covalently modified on the WHB domain (Fig. 1D). The catalytic module contains a RING-type E3 ligase, RBX1, and UbcH5a~Ub (Fig. 1D). RBX1 binds UbcH5a through a canonical RING domain–E2 interface, embracing and activating the ubiquitin in a "closed" conformation (Fig. 1D, fig. S5B) (*41*, *42*, *44-46*). The ternary module, the cullin scaffold, and the catalytic module are interconnected through densely packed interactions (Fig. 1D, fig S5B). For example, (1) the CUL4A N-terminal extension sequence and CR1 domain of CUL4A wrap around the second DDB1 β-propeller fold, BPB, via electrostatic and hydrophobic interactions (*47*), connecting the ternary module and the cullin scaffold (fig. S5B); (2) the C-terminal C/R domain of CUL4A binds RBX1 and the Nedd8 modified on the WHB domain interacts with the UbcH5a backside (*44*), positioning the RBX1/UbcH5a~Ub catalytic module to juxtapose with the substrate IKZF3 in the IMiD-organized ternary module (Fig. 1D, fig S5B).

Pairwise comparisons of the whole complex of these eight ubiquitylation assemblies, each consisting of eight protein subunits and approximately 2,600 amino acid residues, revealed Cα root mean square deviation (RMSD) values within a remarkably narrow range, from 0.3 to 0.9 Å (Fig. 1E, fig. S6A). Alignments of the ternary module, the cullin scaffold, or the catalytic module also yielded similarly low Cα RMSD values (Fig. 1E). These results indicate that the structures of the $_{N8}$CRL4$^{CRBN}$–IMiD–IKZF3 ubiquitylation assemblies exhibit a high degree of conformational conservation, despite the structural differences among the IMiD molecules.

**IMiDs-dependent ternary complex is tightly packed into active ubiquitination assemblies through conformational plasticity of the $_{N8}$CRL4$^{CRBN}$ ligase**

In eight active ubiquitylation assemblies, we observed a consistently multi-layered, close packing in the IMiD binding region and the substrate ubiquitylation region (Fig. 2A). In the IMiD binding region, all eight IMiD molecules simultaneously bind to both the CRBN TBD domain and the IKZF3 ZF2 degron through the phthalimide/glutarimide cores (Figs. 2B, 2C), juxtaposing the K166 of IKZF3, the UbcH5a catalytic cysteine, and the ubiquitin C-terminus in the substrate ubiquitylation region (fig. S6B). Notably, in all eight structures, the spatial distances between the Cα atoms of these residues (IKZF3 K166, UbcH5a C85, and Ub G75) meet the requirements for the chemical bonds and atomic arrangement in the native transition state intermediate of the ubiquitin transfer reaction (figs. S6C, S6D).

The CUL4A-interacting β-propeller BPB of DDB1, previously reported to adopt "hinged", "linear", or "twisted" conformations in apo CRBN/DDB1 complexes (*24*), consistently adopts the "hinged" conformation in all eight structures (fig. S7A). A comparison of the CRBN conformations in our $_{N8}$CRL4A$^{CRBN}$–mezigdomide–IKZF3 complex (hereafter, the Mezig complex) and an IKZF1–mezigdomide–CRBN/DDB1 ternary complex (PDB 8D7Z) (*24*) revealed that while CRBN maintains its DDB1-buried HB domain almost unchanged, the IMiD-binding TBD and Lon domains undergo co-directional movements (fig. S7B). Structural comparisons between previously reported binary/ternary complexes (Fig. 2D) and the ubiquitylation complexes of six IMiDs (excluding golcadomide and cemsidomide, for which no structural data of binary/ternary complexes are available) reveal that both the TBD and Lon domains of CRBN undergo stepwise displacements (Fig. 2E), reflecting their role in coordinating substrate positioning during ubiquitylation.

As a multi-subunit E3 ligase complex, CRL4A E3 ligase exhibits a modular architecture that allows it to adopt distinct states (*48*). For example, the CRL4A$^{DDB1/SV5V}$ complex (PDB 2HYE) (*47*) represents an inactive state lacking Nedd8, E2~Ub, and substrate; the CRL4A$^{DDB1/DDB2}$–DNA complex (PDB 4A0K) (*49*) binds a substrate-related DNA-duplex; and the Nedd8-activated $_{N8}$CRL4A$^{DDB1/CSA}$–UVSSA–E2–Ub complex (PDB 8B3G) (*45*) is fully loaded with E2~Ub and substrate (fig. S7C). The alignment of these structures with our ubiquitylation catalytic intermediate-mimicking Mezig complex reveals substantial conformational flexibility of stepwise rotations or displacements of the DDB1 BPA domain (fig. S7D, S7F), the RBX1/E2~Ub catalytic module (fig. S7E, S7G), the WHB domain and the C/R domain of CUL4A (figs. S7H, 7I). These conformational changes match the steps of substrate binding (PDB 4A0K), Nedd8 activation/E2~Ub loading (PDB 8B3G), and ubiquitin transfer (the Mezig structure), starting from the CRL4A$^{DDB1/SV5-V}$ complex (PDB 2HYE, figs. S7C–S7E).

**"Next-generation" IMiDs bind a cryptic gluing-driven interfacial (GDI) pocket formed by the ZF3 motif and the CRBN Lon domain**

Structural analysis of the eight complexes unexpectedly revealed that four IMiDs, iberdomide, mezigdomide, golcadomide, and cemsidomide, which exhibit strong IKZF3 degradation potency, engage both the degron motif ZF2 and the non-degron motif ZF3 of IKZF3 (Fig. 3A, fig. S8). The refined cryo-EM densities supported the atomic modeling of the IKZF3 non-degron motif ZF3 (Fig. 3B), which had not been observed in previous structures of the ternary complex containing mezigdomide or iberdomide (Fig. 3C) (*24*). The IKZF3 non-degron motif ZF3, which serves as a "proteinaceous glue", fills the groove near the IMiD binding region and the substrate ubiquitylation region formed by the CRBN Lon domain and RBX1 (Fig. 3A, fig. S8). The involvement of IKZF3 ZF3 in contact with the CRBN Lon domain echoes the previous observation that the deletion of ZF3 from the ZF2–ZF3 construct results in a tenfold decrease in binding affinity for the IMiD–CRBN complex (*28*). Interestingly, a previously reported ternary complex structure (PDB 8DEY) (*23*), which contains another Ikaros family transcription factor IKZF2, whose tandem ZF2–ZF3 domains share 91.2% sequence identity with those of IKZF3 (fig. S1F), has revealed an alternative conformation of ZF3 (fig. S8B). Superposition of the IKZF2 ternary complex with our Mezig structure revealed an ~100 ° angular difference between the ZF3 motifs of IKZF2 and IKZF3. When modeled into the mezigdomide-organized ubiquitylation assembly, the IKZF2 ZF3 would clash with UbcH5a (fig. S8B). These findings demonstrate that resolving the full $CRL4^{CRBN}$ ubiquitylation complex is essential for accurately capturing critical neosubstrate features, such as the ZF3 motif, which could otherwise be obscured or misrepresented in ternary complexes.

In the ubiquitylation assembly, the ZF3 motif and the CRBN Lon domain enclose a pocket at the protein–protein interface (Fig. 3A). In contrast to the canonical TBD binding pocket, this distinct interfacial pocket only becomes apparent only upon the IMiD-induced binding of IKZF3 to CRBN during the substrate ubiquitylation process. We thus defined this cryptic pocket as a gluing-driven interfacial (GDI) pocket. In all eight IMiD-organized ubiquitylation assemblies, the phthalimide/glutarimide cores of IMiDs conservatively bind to the canonical CRBN TBD pocket, making contacts with the CRBN aromatic residues H353, W380, W386, and W400 (Figs. 3D, 3G, 3H). The only side-chain interaction between IKZF3 ZF2 and IMiDs is formed by IKZF3 Q147 (Figs. 3E, 3G, 3H), whose substitution with histidine (Q147H) results in IMiD resistance (*7*). Intriguingly, the additional groups of the "next-generation" IMiDs (mezigdomide, iberdomide, golcadomide, and cemsidomide) reach the GDI pocket juxtaposed with the TBD pocket, making contacts with IKZF3 R186 and hydrophobic amino acid residues (e.g., H103, F102, and F150) on the CRBN Lon domain (Figs. 3F, 3G, 3H). Based on their binding modes with the TBD or GDI pockets, the eight IKZF3-targeting IMiDs can be classified into two categories: monovalent IMiDs

(MvIMiDs, fig. S9A), which bind exclusively to the TBD pocket (e.g., pomalidomide, thalidomide, lenalidomide, and avadomide), and bridging IMiDs (BdIMiDs, fig. S9B), which simultaneously engage both the TBD and GDI pockets to introduce additional drug–protein interactions (e.g., mezigdomide, iberdomide, golcadomide, and cemsidomide).

We performed IKZF3 degradation assays in cells and mutagenesis-based *in vitro* ubiquitylation assays to validate our structural observation that the IKZF3 ZF3 motif contributes to GDI pocket formation, and to investigate how the IMiD–GDI pocket interaction influences IKZF3 ubiquitylation and degradation. HEK293T cells transfected with IKZF3 (IKZF3$^{FL}$ construct) or IKZF3 deletion constructs were treated with 1 μM of either pomalidomide or mezigdomide for 8 hours, and the intracellular abundance of IKZF3 was assessed by western blot (WB, Fig. 3I). The deletion of the IKZF3 degron motif ZF2 (amino acid residues 142–169) (IKZF3$^{\Delta ZF2}$ construct) rendered IKZF3 resistant to IMiD treatment, effectively serving as a reliable negative control (Fig. 3I). Notably, the deletion of the IKZF3 non-degron motif ZF3 (amino acid residues 171–198) (IKZF3$^{\Delta ZF3}$ construct) also resulted in IMiD resistance, although to a lesser extent than the IKZF3$^{\Delta ZF2}$ construct did (Fig. 3I). These *in vivo* results agree with the findings from previous cellular IKZF1/3 zinc finger deletion degradation assays that deletion of ZF3 impaired IMiD-induced IKZF3 degradation using fluorescent reporter vectors (*28*). The substitution of the IKZF3 residue R186 with alanine (R186A) impaired IKZF3 ubiquitylation induced by mezigdomide *in vitro* (Fig. 3J), suggesting that the R186A mutation disrupts additional drug–protein interactions within the GDI pocket. Our *in vitro* data were further substantiated by previous results that the mutation of this consensus arginine residue in Ikaros family transcription factors (IKZF3 R186 and IKZF1 R185) impairs the binding affinity of ZF2–ZF3 construct to the IMiD–CRBN complex (*28*). The Lon domain side of the GDI pocket centers on residue H103 (fig. S10A) and includes a hydrophobic surface (figs. S10B, S10C) that synergistically recruits MGDs and zinc finger proteins (fig. S10D) (*18, 22*). The incorporation of the CRBN H103A mutant into the $_{N8}$CRL4$^{CRBN}$ ligase complex impaired IMiD-induced IKZF3 ubiquitylation (Fig. 3K).

Together, our structural and biochemical findings reveal that the IKZF3 non-degron motif ZF3 glues the CRBN Lon domain and RBX1/UbcH5a catalytic module to form a cryptic GDI pocket and that the IMiD–GDI pocket interactions provide an unexpected mechanistic rationale for the enhanced efficacy of BdIMiDs compared to that of MvIMiDs.

## Understanding IMiD efficacy through IMiD–GDI pocket interactions in the full CRL4$^{CRBN}$ ubiquitylation complex

Although IMiDs all share phthalimide/glutarimide core structures, different IMiDs have been shown to reshape the CRBN to selectively recognize distinct proteins, such as IKZF3, GSPT1, and

CK1α (*12*). We conducted *in silico* docking of a panel of previously reported IMiDs with distinct substrate selectivities (*19, 27, 30, 31, 50-55*) into the fully assembled $CRL4^{CRBN}$ ubiquitylation complex using the Schrödinger Maestro software (Fig. 4A, fig. S11). The analysis revealed that: (1) all eight IKZF3-targeting IMiDs characterized in this study exhibited relatively low (and thus more favorable) docking scores (Fig. 4A); (2) the four BdIMiDs with enhanced IKZF3 selectivity and degradation potency showed significantly lower scores than the MvIMiDs, with mezigdomide achieving the most favorable score (Fig. 4A); and (3) IMiDs selective for other neosubstrates such as GSPT1 or CK1α, as well as promiscuous degraders, generally yielded relatively unfavorable docking scores (Fig. 4A). However, performing the same *in silico* analysis using the previously reported ternary complex (PDB 8D7Z) failed to recapitulate these results (Fig. 4A).

The therapeutic efficacy of IMiDs encompasses both substrate selectivity and degradation potency. We performed a correlation analysis by plotting the logarithm of IKZF3 degradation potency for the eight IKZF3-targeting IMiDs against their docking scores. Using the $CRL4^{CRBN}$ full ubiquitylation complex, linear regression yielded an $R^2$ of 0.74, with a Pearson's correlation coefficient (r) of 0.85 and a Spearman's correlation coefficient (ρ) of 0.91 (Fig. 4B). By contrast, the ternary complex model (PDB 8D7Z) resulted a markedly lower $R^2$ of 0.30, with negative $r = -0.55$ and $\rho = -0.48$ (Fig. 4C). We further strengthened the application of our discovery of the IMiD–GDI pocket interaction in the full ubiquitylation complex for understanding the structure–activity relationship (SAR) of mezigdomide analogs. Based on SAR data from the mezigdomide development study (*37*), docking scores from the full ubiquitylation complex showed a strong positive correlation with IKZF3 degradation potency (Fig. 4D), while in contrast, docking scores from the ternary complex model (PDB 8D7Z) showed a poor correlation (Fig. 4E). These molecular docking analyses revealed that enhanced drug–GDI pocket compatibility correlates with improved efficacy (fig. S12), suggesting a previously unrecognized strategy for the SAR optimization of IMiDs.

We further selected three representative IMiDs with distinct substrate selectivities for structural analysis. In our resolved Mezig structure, the GDI pocket formed by the IKZF3 ZF3 motif and CRBN Lon domain is optimally accommodated by the terminal 2-fluoro-4-cyanophenyl group of mezigdomide, establishing extra drug–protein interactions (Fig. 4F). However, in the docking models, the GSPT1-selective degrader eragidomide (*27*) (Fig. 4G) or the CK1α-selective degrader SJ3149 (*19*) (Fig. 4H) could not be accommodated within the GDI pocket. These analyses indicate that steric or chemical incompatibility with the GDI pocket can hinder effective IMiD engagement in the full ubiquitylation machinery, thereby influencing substrate selectivity.

Collectively, our results show that *in silico* docking with the full $CRL4^{CRBN}$ ubiquitylation complex enables clear discrimination of IKZF3-targeting IMiDs and elucidation of SAR via the IMiD–GDI pocket interplay, insights unattainable from the ternary complexes.

## Discussion

Thalidomide, a historic milestone in medical science, was initially notorious for its severe teratogenic effects (*1*) but was subsequently repurposed as an effective therapy for multiple myeloma (*56*). Thalidomide-derived IMiDs are now considered the most successful targeted protein degradation drugs both for clinical treatment and market application (*6*), exerting therapeutic effects by reprogramming the substrate selectivity of the CRL4$^{CRBN}$ E3 ubiquitin ligase (*3-5*) and degrading disease-associated proteins, such as IKZF1 and IKZF3 (*7-9*). In the present study, leveraging activity-based trapping chemistry (*41-43*), we provide the first comprehensive molecular portrait of how IMiDs engage the intact, catalytically active CRL4$^{CRBN}$ ubiquitylation machinery to induce neosubstrate ubiquitylation, thereby advancing beyond previous mechanistic insights gained from partial ternary complexes.

Our cryo-EM structures of eight catalytically active $_{N8}$CRL4A$^{CRBN}$–IKZF3–E2–Ub complexes induced by distinct IMiDs reveal a conserved architecture of the ubiquitylation machinery driving neosubstrate modification. Structural and functional analyses revealed that the non-degron ZF3 motif of IKZF3 plays an unexpected regulatory role, acting as a "proteinaceous glue" to reinforce the compact architecture of the ubiquitylation region and enhance IMiD-induced ubiquitylation efficiency. Compared to ternary complexes lacking the activated $_{N8}$CRL4$^{CRBN}$ E3 ligase or E2~Ub conjugates, where ZF3 is either unresolved (*24*) or differently positioned (*23*), our fully assembled ubiquitylation complexes reveal that ZF3 adopts a distinct conformation, positioned between the CRBN Lon domain and the RBX1/E2~Ub catalytic module (Fig. 4I). This arrangement enables the formation of a previously unrecognized GDI pocket that enhances IMiD binding (Fig. 4I). Relative to MvIMiDs (e.g., pomalidomide, thalidomide, lenalidomide, and avadomide), which bind only the CRBN TBD pocket (Fig. 4J), BdIMiDs (e.g., mezigdomide, iberdomide, golcadomide, and cemsidomide) engage both TBD and GDI pockets (Fig. 4K), forming additional interactions that enhance degradation potency and target selectivity. Furthermore, *in silico* docking using the fully assembled CRL4$^{CRBN}$ ubiquitylation complex enables differentiation of IKZF3-targeting IMiDs and facilitates SAR interpretation through the newly uncovered IMiD–GDI pocket interactions, which are not achievable with previous ternary complex models. Together, these findings highlight the importance of resolving the full ubiquitylation machinery structure to provide a more comprehensive mechanistic basis for understanding IMiDs' efficacy and selectivity.

To date, the vast majority of CRBN-based molecular glue degraders (MGDs) exploit the canonical and conserved phthalimide/glutarimide–TBD pocket interaction (*16-33*), restricting the chemical space available for modulating substrate selectivity or minimizing off-target effects through structure-based molecular design. Our findings reveal a comprehensive structural view of the IMiD-organized, fully assembled ubiquitylation machinery and open the possibility of designing

improved MGDs that are tailored to engage the GDI pocket, thereby enabling more efficient and selective targeted substrate ubiquitylation through more tightly organized and catalytically competent ubiquitylation machinery. We anticipate that the newly uncovered interaction between BdIMiDs and the GDI pocket may pave the way for a new paradigm in the structure-guided rational design of improved MGDs.

## References and Notes


1. W. G. McBride, THALIDOMIDE AND CONGENITAL ABNORMALITIES. *The Lancet* **278**, 1358 (1961).
2. J. B. Bartlett, K. Dredge, A. G. Dalgleish, Timeline - The evolution of thalidomide and its IMiD derivatives as anticancer agents. *Nat. Rev. Cancer* **4**, 314-322 (2004).
3. T. Ito *et al.*, Identification of a Primary Target of Thalidomide Teratogenicity. *Science* **327**, 1345-1350 (2010).
4. A. Lopez-Girona *et al.*, Cereblon is a direct protein target for immunomodulatory and antiproliferative activities of lenalidomide and pomalidomide. *Leukemia* **26**, 2326-2335 (2012).
5. M. Jan, A. S. Sperling, B. L. Ebert, Cancer therapies based on targeted protein degradation — lessons learned with lenalidomide. *Nat. Rev. Clin. Oncol.* **18**, 401-417 (2021).
6. J. S. Miguel *et al.*, Pomalidomide plus low-dose dexamethasone versus high-dose dexamethasone alone for patients with relapsed and refractory multiple myeloma (MM-003): a randomised, open-label, phase 3 trial. *Lancet Oncol.* **14**, 1055-1066 (2013).
7. J. Krönke *et al.*, Lenalidomide Causes Selective Degradation of IKZF1 and IKZF3 in Multiple Myeloma Cells. *Science* **343**, 301-305 (2014).
8. G. Lu *et al.*, The Myeloma Drug Lenalidomide Promotes the Cereblon-Dependent Destruction of Ikaros Proteins. *Science* **343**, 305-309 (2014).
9. A. K. Gandhi *et al.*, Immunomodulatory agents lenalidomide and pomalidomide co-stimulate T cells by inducing degradation of T cell repressors Ikaros and Aiolos via modulation of the E3 ubiquitin ligase complex CRL4. *Br. J. Haematol.* **164**, 811-821 (2014).
10. J. Krönke *et al.*, Lenalidomide induces ubiquitination and degradation of CK1a in del(5q) MDS. *Nature* **523**, 183-188 (2015).
11. A. List *et al.*, Efficacy of lenalidomide in myelodysplastic syndromes. *N. Engl. J. Med.* **352**, 549-557 (2005).
12. V. Oleinikovas, P. Gainza, T. Ryckmans, B. Fasching, N. H. Thomä, From Thalidomide to Rational Molecular Glue Design for Targeted Protein Degradation. *Annu. Rev. Pharmacol. Toxicol.* **64**, 291-312 (2024).
13. M. Konstantinidou, M. R. Arkin, Molecular glues for protein-protein interactions Progressing toward a new dream. *Cell Chem. Biol.* **31**, 1064-1088 (2024).
14. J. M. Tsai, R. P. Nowak, B. L. Ebert, E. S. Fischer, Targeted protein degradation: from mechanisms to clinic. *Nat. Rev. Mol. Cell Biol.* **25**, 740-757 (2024).
15. S. J. Hughes, A. Ciulli, Molecular recognition of ternary complexes: a new dimension in the structure-guided design of chemical degraders. *Essays Biochem.* **61**, 505-516 (2017).
16. Y. Chrisochoidou *et al.*, Evaluating the impact of CRBN mutations on response to immunomodulatory drugs and novel CRBN-binding agents in myeloma. *Blood*, (2025).
17. P. Y. Ting *et al.*, A molecular glue degrader of the WIZ transcription factor for fetal hemoglobin induction. *Science* **385**, 91-99 (2024).
18. J. A. M. Mercer *et al.*, Continuous evolution of compact protein degradation tags regulated by selective molecular glues. *Science* **383**, eadk4422 (2024).
19. G. Nishiguchi *et al.*, Selective CK1α degraders exert antiproliferative activity against a broad range of human cancer cell lines. *Nat. Commun.* **15**, 482 (2024).
20. A. Kroupova *et al.*, Design of a Cereblon construct for crystallographic and biophysical studies of protein degraders. *Nat. Commun.* **15**, 8885 (2024).

21. J. R. Kerrigan *et al.*, Discovery and Optimization of First-in-Class Molecular Glue Degraders of the WIZ Transcription Factor for Fetal Hemoglobin Induction to Treat Sickle Cell Disease. *J. Med. Chem.* **67**, 20682-20694 (2024).
22. X. Ma *et al.*, Structural and biophysical comparisons of the pomalidomide- and CC-220-induced interactions of SALL4 with cereblon. *Sci. Rep.* **13**, 22088 (2023).
23. S. Bonazzi *et al.*, Discovery and characterization of a selective IKZF2 glue degrader for cancer immunotherapy. *Cell Chem. Biol.* **30**, 235-247.e212 (2023).
24. E. R. Watson *et al.*, Molecular glue CELMoD compounds are regulators of cereblon conformation. *Science* **378**, 549-553 (2022).
25. H. Furihata *et al.*, Structural bases of IMiD selectivity that emerges by 5-hydroxythalidomide. *Nat. Commun.* **11**, 4578 (2020).
26. M. E. Matyskiela *et al.*, Crystal structure of the SALL4-pomalidomide-cereblon-DDB1 complex. *Nat. Struct. Mol. Biol.* **27**, 319-322 (2020).
27. C. Surka *et al.*, CC-90009, a novel cereblon E3 ligase modulator, targets acute myeloid leukemia blasts and leukemia stem cells. *Blood* **137**, 661-677 (2021).
28. Q. L. Sievers *et al.*, Defining the human C2H2 zinc finger degrome targeted by thalidomide analogs through CRBN. *Science* **362**, eaat0572 (2018).
29. M. E. Matyskiela *et al.*, A Cereblon Modulator (CC-220) with Improved Degradation of Ikaros and Aiolos. *J. Med. Chem.* **61**, 535-542 (2018).
30. M. E. Matyskiela *et al.*, A novel cereblon modulator recruits GSPT1 to the CRL4(CRBN) ubiquitin ligase. *Nature* **535**, 252-257 (2016).
31. G. Petzold, E. S. Fischer, N. H. Thomä, Structural basis of lenalidomide-induced CK1α degradation by the CRL4CRBN ubiquitin ligase. *Nature* **532**, 127-130 (2016).
32. P. P. Chamberlain *et al.*, Structure of the human Cereblon-DDB1-lenalidomide complex reveals basis for responsiveness to thalidomide analogs. *Nat. Struct. Mol. Biol.* **21**, 803-809 (2014).
33. E. S. Fischer *et al.*, Structure of the DDB1-CRBN E3 ubiquitin ligase in complex with thalidomide. *Nature* **512**, 49-53 (2014).
34. M. M. Hassan *et al.*, Exploration of the tunability of BRD4 degradation by DCAF16 trans-labelling covalent glues. *Eur. J. Med. Chem.* **279**, 116904 (2024).
35. P. R. Hagner *et al.*, CC-122, a pleiotropic pathway modifier, mimics an interferon response and has antitumor activity in DLBCL. *Blood* **126**, 779-789 (2015).
36. C. C. Bjorklund *et al.*, Iberdomide (CC-220) is a potent cereblon E3 ligase modulator with antitumor and immunostimulatory activities in lenalidomide- and pomalidomide-resistant multiple myeloma cells with dysregulated CRBN. *Leukemia* **34**, 1197-1201 (2020).
37. J. D. Hansen *et al.*, Discovery of CRBN E3 Ligase Modulator CC-92480 for the Treatment of Relapsed and Refractory Multiple Myeloma. *J. Med. Chem.* **63**, 6648-6676 (2020).
38. S. Carrancio *et al.*, CC-99282 is a Novel Cereblon (CRBN) E3 Ligase Modulator (CELMoD) Agent with Enhanced Tumoricidal Activity in Preclinical Models of Lymphoma. *Blood* **138**, 1200-1200 (2021).
39. J.-M. Michot *et al.*, Clinical Activity of CC-99282, a Novel, Oral Small Molecule Cereblon E3 Ligase Modulator (CELMoD) Agent, in Patients (Pts) with Relapsed or Refractory Non-Hodgkin Lymphoma (R/R NHL) - First Results from a Phase 1, Open-Label Study. *Blood* **138**, 3574-3574 (2021).

40. S. Perino *et al.*, CFT7455, a Novel IKZF1/3 Degrader, Demonstrates Potent Anti-Tumor Activity in Models of Non-Hodgkin's Lymphoma As a Single Agent or in Combination with Clinically Approved Agents. *Blood* **140**, 11575-11575 (2022).
41. J. Li *et al.*, Cullin-RING ligases employ geometrically optimized catalytic partners for substrate targeting. *Mol. Cell* **84**, 1304-1320 e1316 (2024).
42. J. Liwocha *et al.*, Mechanism of millisecond Lys48-linked poly-ubiquitin chain formation by cullin-RING ligases. *Nat. Struct. Mol. Biol.* **31**, 378-389 (2024).
43. G. A. Davidson, Z. Moafian, A. R. Sensi, Z. Zhuang, Thioether-mediated protein ubiquitination in constructing affinity- and activity-based ubiquitinated protein probes. *Nat. Protoc.* (2025). https://doi.org/10.1038/s41596-025-01162-8
44. K. Baek *et al.*, NEDD8 nucleates a multivalent cullin-RING-UBE2D ubiquitin ligation assembly. *Nature* **578**, 461-466 (2020).
45. G. Kokic *et al.*, Structural basis for RNA polymerase II ubiquitylation and inactivation in transcription-coupled repair. *Nat. Struct. Mol. Biol.* **31**, 536–547 (2024).
46. L. Cappadocia, C. D. Lima, Ubiquitin-like Protein Conjugation: Structures, Chemistry, and Mechanism. *Chem. Rev.* **118**, 889-918 (2018).
47. S. Angers *et al.*, Molecular architecture and assembly of the DDB1-CUL4A ubiquitin ligase machinery. *Nature* **443**, 590-593 (2006).
48. M. D. Petroski, R. J. Deshaies, Function and regulation of cullin–RING ubiquitin ligases. *Nat. Rev. Mol. Cell Biol.* **6**, 9-20 (2005).
49. Eric S. Fischer *et al.*, The Molecular Basis of CRL4DDB2/CSA Ubiquitin Ligase Architecture, Targeting, and Activation. *Cell* **147**, 1024-1039 (2011).
50. J. Zou *et al.*, The novel protein homeostatic modulator BTX306 is active in myeloma and overcomes bortezomib and lenalidomide resistance. *J. Mol. Med.* **98**, 1161-1173 (2020).
51. G. Nishiguchi *et al.*, Identification of Potent, Selective, and Orally Bioavailable Small-Molecule GSPT1/2 Degraders from a Focused Library of Cereblon Modulators. *J. Med. Chem.* **64**, 7296-7311 (2021).
52. C. E. Powell *et al.*, Selective Degradation of GSPT1 by Cereblon Modulators Identified via a Focused Combinatorial Library. *ACS Chem. Biol.* **15**, 2722-2730 (2020).
53. M. Teng *et al.*, Development of PDE6D and CK1α Degraders through Chemical Derivatization of FPFT-2216. *J. Med. Chem.* **65**, 747-756 (2022).
54. S.-M. Park *et al.*, Dual IKZF2 and CK1α degrader targets acute myeloid leukemia cells. *Cancer Cell* **41**, 726-739.e711 (2023).
55. L. Huang *et al.*, Development of Oral, Potent, and Selective CK1α Degraders for AML Therapy. *JACS Au* **4**, 4423-4434 (2024).
56. S. Singhal *et al.*, Antitumor Activity of Thalidomide in Refractory Multiple Myeloma. *N. Engl. J. Med.* **341**, 1565-1571 (1999).

**Acknowledgments:** We acknowledge the Tsinghua University Branch of China National Center for Protein Sciences (Beijing) and Shuimu BioSciences (Hangzhou) for cryo-EM data screening and collection. We thank the Center of Protein Analysis Technology, Tsinghua University, for MS analysis. Z. D. thanks the support from Shuimu Tsinghua Scholars Program.

**Funding:**

National Natural Science Foundation of China 92253302 (L.L.)

National Natural Science Foundation of China T2488301 (L.L.)

National Natural Science Foundation of China 22137005 (L.L.)

National Natural Science Foundation of China 22227810 (L.L.)

National Natural Science Foundation of China 22277073 (M.P.)

National Natural Science Foundation of China 92253302 (M.P.)

National Key R&D Program of China 2022YFC3401500 (L.L.)

National Key R&D Program of China 2023YFA0915300 (M.P.)

New Cornerstone Science Foundation (L.L.)

Shanghai Rising-Star Program 22QA1404900 (M.P.)

Shanghai Pilot Program for Basic Research, Shanghai Jiao Tong University 21TQ1400224 (M.P.)

Foundation of Muyuan Laboratory 118602240 (M.P.)

Fundamental Research Funds for the Central University (M.P.).

Shanghai Jiao Tong University 2030 Initiative WH510363003/003 (M.P.)

Shanghai Frontiers Science Center of Drug Target Identification and Delivery ZXWH2170101 (H.A.)

**Author contributions:**

Conceptualization: L.L., M.P., H.A., and Z.D. Chemical trapping methodology: Z.D. and Q.S. Cloning and protein purification: Z.D., Q.S., J.L., Z.H., L.Z., S.T., W.H., and Q.Z. Cryo-EM sample preparation: Z.D. Cryo-EM data processing: H.A. Model building: Z.D. and H.A. Ubiquitylation and degradation assays: Z.D., Q.S., and J.L. Molecular docking: Z.D., J.Z., and H.L. Data interpretation: Z.D. and H.A. Visualization: Z.D. Funding acquisition: L.L., M.P., and H.A. Supervision: L.L. Writing – original draft: Z.D., M.P., and H.A. Writing – review & editing: L.L., M.P., H.A., and Z.D.

**Competing interests:** Authors declare that they have no competing interests.

**Data and materials availability:** Coordinates and cryo-EM maps of IMiD-organized complexes have been deposited in the Protein Data Bank (PDB) and Electron Microscopy Data Bank (EMDB), including the thalidomide complex (PDB 9UUQ, EMD-64515), the lenalidomide complex (9V09, EMD-64658), the pomalidomide complex (9V0A, EMD-64659), the avadomide complex (9V0B, EMD-64660), the iberdomide complex (9V0C, EMD-64661), the mezigdomide complex (9UUM, EMD-64512), the golcadomide complex (9V0E, EMD-64662), and the cemsidomide complex (9V0F, EMD-64663). Newly created materials from this study may be requested from the corresponding authors. Source data are provided with this paper.

**Supplementary Materials**

Materials and Methods

Figs. S1 to S12

Tables S1 to S3

References (*58–65*)

Data S1 to S3

**Fig. 1. Structural visualization of $_{N8}$CRL4$^{CRBN}$ E3 ligase-mediated IKZF3 ubiquitylation induced by eight approved and clinical IMiDs.** (**A**) Colored domain scheme of subunits with the catalytically active CRL4$^{CRBN}$ ubiquitylation assembly. The chemical crosslink between Ub C-terminus, IKZF3 K166, and UbcH5a active site is indicated by lines. (**B**) Cryo-EM maps representing eight IKZF3-targeting IMiDs in complex with IKZF3 and E2~Ub loaded $_{N8}$CRL4$^{CRBN}$ ligase with the active ubiquitylation assembly. Chemical structures, cartoon models, and cryo-EM densities of eight individual IMiDs are shown. (**C**) Cartoon model of the mezigdomide-organized ubiquitylation assembly with subcomponents indicated. (**D**) Architectures of the ternary module, the cullin scaffold, and the catalytic module in the mezigdomide-organized ubiquitylation assembly. (**E**) Heat map graphs showing Cα RMSDs of the whole complex, the ternary module, the cullin scaffold, and the catalytic module by pairwise alignments of eight structures.

**Fig. 2. Conserved binding mode of eight IMiDs in inducing neosubstrate ubiquitylation.** (**A**) A close-up view of the IMiD binding region and substrate ubiquitylation region in eight IMiD-organized ubiquitylation assemblies. (**B**) Guide to viewing the IMiD binding regions and substrate ubiquitylation regions shown in **C**. (**C**) Close-up views showing the binding mode of eight IMiDs. (**D**) Cartoon diagram illustrating the pathway for IMiD-organized complex assembly and summary of reported PDB structures of binary or ternary complexes containing eight IMiDs studied here. (**E**) Structural alignments of individual IMiD-organized binary complex (colored white), ternary complex (colored gray), and ubiquitylation assembly (colored as **Fig. 1A** indicates), highlighting the conformational changes of CRBN TBD and Lon domains.

**Fig. 3. A cryptic GDI pocket formed by the IKZF3 non-degron motif ZF3 and CRBN Lon domain contributes to IMiD-induced IKZF3 ubiquitylation and degradation.** (**A**) A close-up view of the Mezig structure with a cartoon model fit into the cryo-EM map. The red dashed circle indicates the unexpected IKZF3 ZF3 density. (**B**) Two orientations of the IKZF3 cryo-EM density in the Mezig structure with cartoon model fit. (**C**) Comparison of tandem ZF2–ZF3 motifs observed in mezigdomide- or iberdomide-organized ubiquitylation assemblies (top, this work) and ternary complexes (PDB 8D7Z, 8D80), revealing the absence of ZF3 density in ternary complexes. The ZF2–ZF3 motifs in ubiquitylation assemblies are shown as semi-transparent cryo-EM densities with cartoon model fit. The ZF2 motifs in ternary complexes (PDB 8D7Z, 8D80) are shown as semi-transparent cartoon surfaces and models. (**D**) Detailed view of mezigdomide binding in the CRBN TBD pocket. Key TBD pocket residues, CRBN W380, W386, and W400, are indicated. (**E**) Detailed view of mezigdomide interacting with CRBN and IKZF3. Key interacting residues, CRBN F150, H353, H378, W386, and IKZF3 Q147 are indicated. (**F**) Detailed view of mezigdomide interacting with the IKZF3–CRBN GDI pocket. Key interacting residues, CRBN F102, H103, F150, I152, and IKZF3 R186, are indicated. Cryo-EM density map and atomic model are shown. (**G**, **H**) Zoomed-in views of each IMiD molecule binding in the CRBN TBD pocket or GDI pocket. Side chains of key interacting amino acid residues are shown as stick models (top). Surface representations of CRBN and IKZF3 are used to highlight the structural features of the binding pockets. (**I**) A representative western blot image (top) of *in vivo* degradation assay using IKZF3$^{FL}$, IKZF3$^{\Delta ZF2}$, or IKZF3$^{\Delta ZF3}$ construct and bar graph showing quantified IKZF3 degradation data from $n$ = 2 technical replicates (bottom). (**J**) *In vitro* ubiquitylation assay using WT IKZF3 ZF2–ZF3 or its R186A mutant in the presence of pomalidomide or mezigdomide. (**K**) *In vitro* ubiquitylation assay using WT CRBN or its H103 mutant with the fully-assembled $_{N8}$CRL4$^{CRBN}$ E3 ligase complex. Bar graph comparing the fraction of unmodified and ubiquitylated IKZF3 species in the presence of eight IMiDs. Data are presented

as mean ± SD from $n$ = 3 technical replicates.

**Fig. 4. The IMiD–GDI pocket interplay in the substrate ubiquitylation process provides a rational understanding of IMiDs' efficacy.** (**A**) Heat map graphs showing docking scores of IMiDs with distinct target selectivities. Mezigdomide-organized full ubiquitylation assembly (Mezig complex) or ternary complex (PDB 8D7Z) was used as the docking model. Low (favorable) and high (unfavorable) docking scores are indicated by blue and red colors. (**B**, **C**) Dot plots showing the correlation analysis of the logarithm of IKZF3 degradation potency [lg(IKZF3 remaining%)] for the eight IKZF3-targeting IMiDs against their docking scores within the full ubiquitylation complex (**B**) or ternary complex (**C**). IKZF3 degradation potency data are from **fig. S1B**. (**D**, **E**) Dot plots showing the correlation analysis of the logarithm of previously reported IKZF3 EC50 [lg(EC50)] for mezigdomide analogs against their docking scores within the full ubiquitylation complex (**D**) or ternary complex (**E**). $R^2$ of the simple linear regression model, Pearson's correlation coefficient (r), and Spearman's correlation coefficient (ρ) are indicated. (**F**) Structural analysis and schematic illustration of mezigdomide engaging both the CRBN TBD and GDI pockets in our cryo-EM structure of full ubiquitylation assembly. (**G**, **H**) Structural analysis and schematic illustration of GSPT1-selective eragidomide (**G**) or CK1α-selective SJ3149 (**H**) docked into our Meizg structure. (**I**) Cartoon diagram illustrating the pathway for the IMiD-organized ternary complex to catalytically active ubiquitylation assembly. Engagement of the fully-assembled $_{N8}CRL4^{CRBN}$ E3 ligase and E2~Ub enables the wobbly IKZF3 ZF3 motif to form the GDI pocket. (**J**, **K**) Cartoon summary illustrating the rationale for understanding the molecular origin of the efficacy of MvIMiDs (**J**) or BdIMiDs (**K**) through IMiD–GDI pocket interplay.

# Figure 1

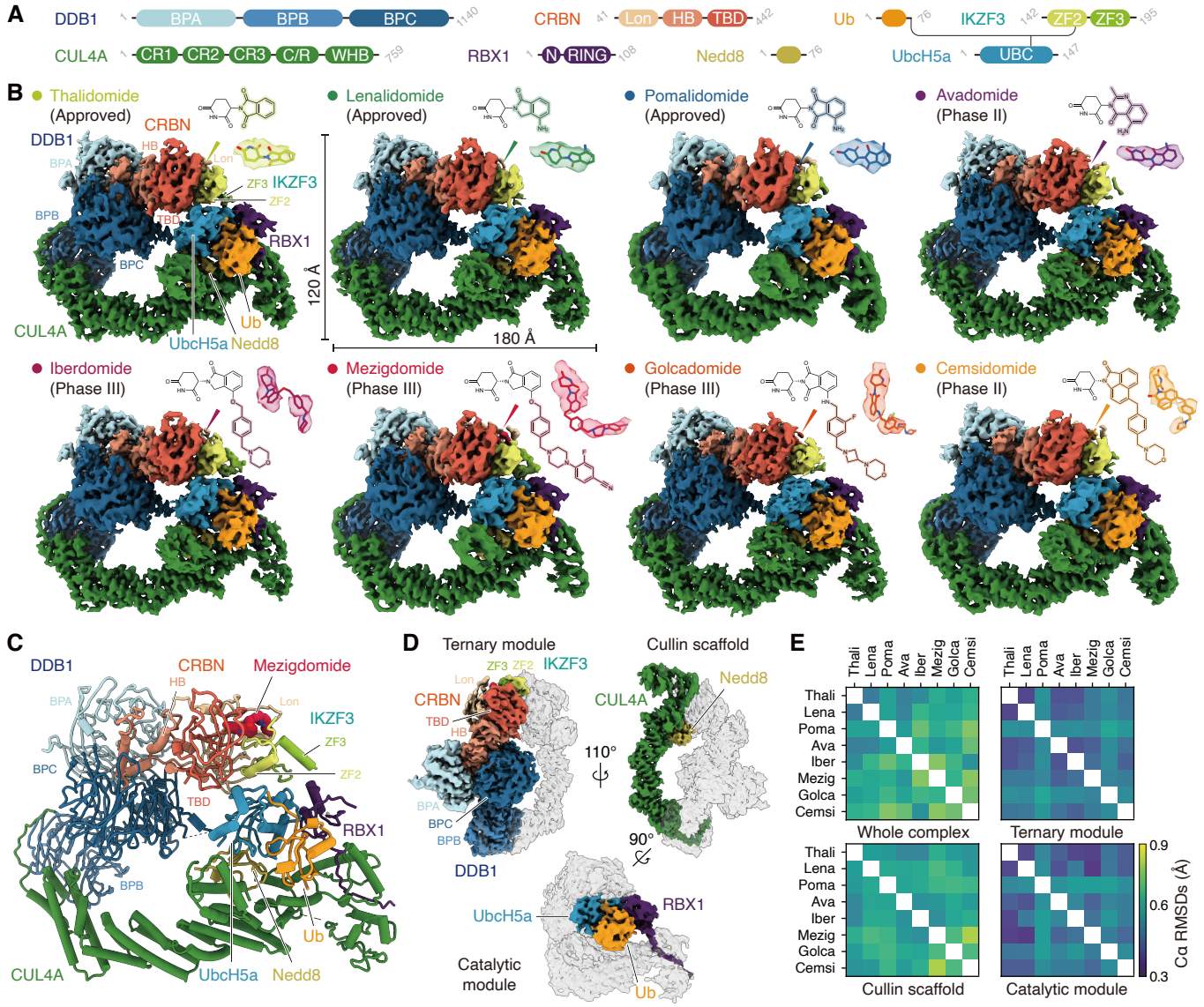
A
DDB1
BPA
BPB
BPC
1140
CRBN
41
Lon
HB
TBD
442
Ub
76
IKZF3
142
ZF2
ZF3
195
CUL4A
CR1
CR2
CR3
C/R
WHB
759
RBX1
N
RING
108
Nedd8
76
UbcH5a
UBC
147
B
Thalidomide (Approved)
Lenalidomide (Approved)
Pomalidomide (Approved)
Avadomide (Phase II)
Iberdomide (Phase III)
Mezigdomide (Phase III)
Golcadomide (Phase III)
Cemsidomide (Phase II)
120 Å
180 Å
C
DDB1
CRBN
Mezigdomide
IKZF3
RBX1
Ub
CUL4A
UbcH5a
Nedd8
D
Ternary module
Cullin scaffold
110°
90°
Catalytic module
E
Thali
Lena
Poma
Ava
Iber
Mezig
Golca
Cemsi
Whole complex
Ternary module
Cullin scaffold
Catalytic module
0.9
0.6
0.3
Cα RMSDs (Å)

**Fig. 1. Structural visualization of $_{N8}$CRL4$^{CRBN}$ E3 ligase-mediated IKZF3 ubiquitylation induced by eight approved and clinical IMiDs.**

(**A**) Colored domain scheme of subunits with the catalytically active CRL4$^{CRBN}$ ubiquitylation assembly. The chemical crosslink between Ub C-terminus, IKZF3 K166, and UbcH5a active site is indicated by lines.

(**B**) Cryo-EM maps representing eight IKZF3-targeting IMiDs in complex with IKZF3 and E2~Ub loaded $_{N8}$CRL4$^{CRBN}$ ligase with the active ubiquitylation assembly. Chemical structures, cartoon models, and cryo-EM densities of eight individual IMiDs are shown.

(**C**) Cartoon model of the mezigdomide-organized ubiquitylation assembly with subcomponents indicated.

(**D**) Architectures of the ternary module, the cullin scaffold, and the catalytic module in the mezigdomide-organized ubiquitylation assembly.

(**E**) Heat map graphs showing Cα RMSDs of the whole complex, the ternary module, the cullin scaffold, and the catalytic module by pairwise alignments of eight structures.

# Figure 2

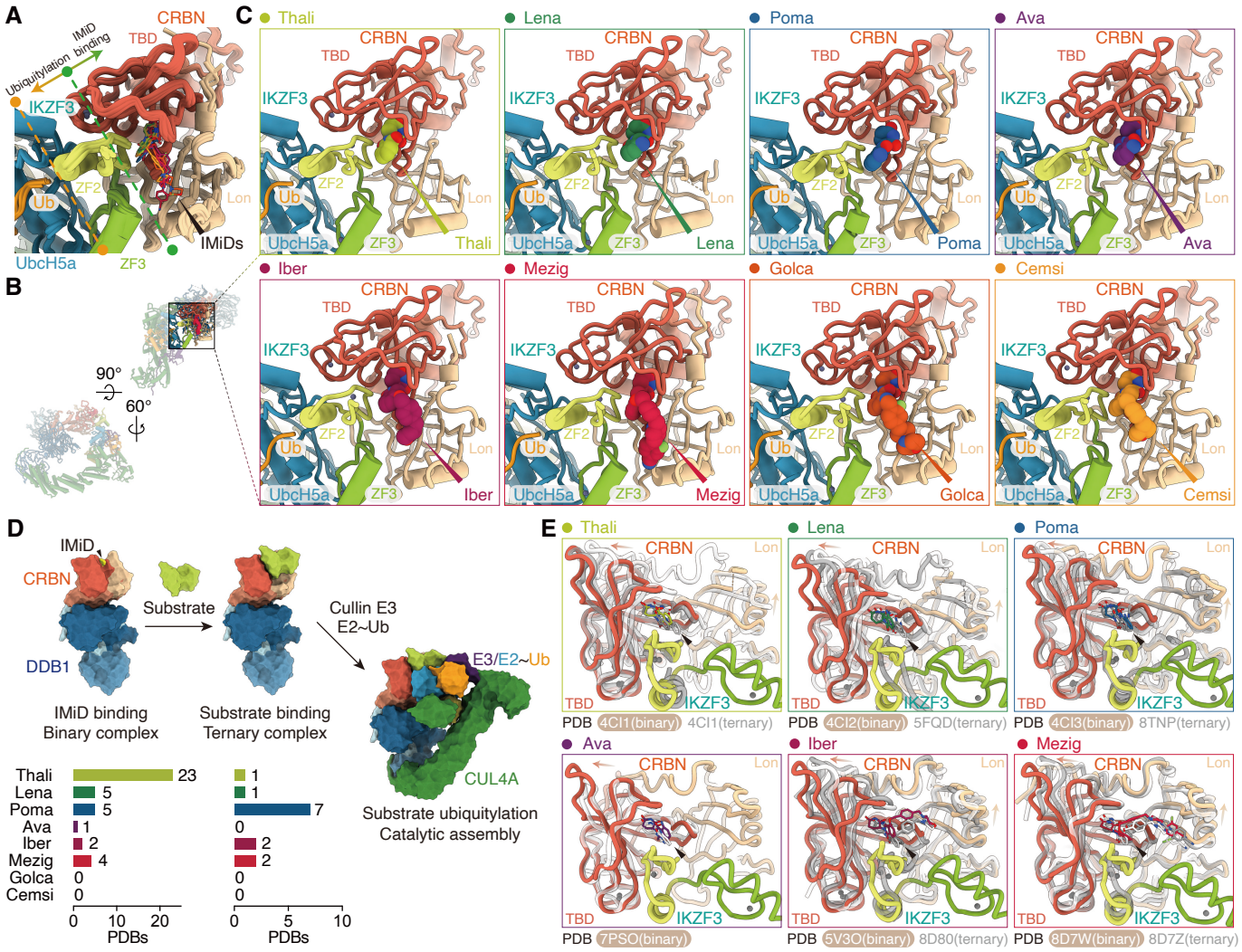
A
CRBN
TBD
IMiD binding
Ubiquitylation
IKZF3
ZF2
Ub
Lon
IMiDs
UbcH5a
ZF3
B
90°
60°
C
Thali
Lena
Poma
Ava
Iber
Mezig
Golca
Cemsi
D
IMiD
CRBN
DDB1
Substrate
IMiD binding
Binary complex
Substrate binding
Ternary complex
Cullin E3
E2~Ub
E3/E2~Ub
CUL4A
Substrate ubiquitylation
Catalytic assembly
Thali 23 1
Lena 5 1
Poma 5 7
Ava 1 0
Iber 2 2
Mezig 4 2
Golca 0 0
Cemsi 0 0
0 10 20
PDBs
0 5 10
PDBs
E
PDB 4CI1(binary) 4CI1(ternary)
PDB 4CI2(binary) 5FQD(ternary)
PDB 4CI3(binary) 8TNP(ternary)
PDB 7PSO(binary)
PDB 5V3O(binary) 8D80(ternary)
PDB 8D7W(binary) 8D7Z(ternary)

**Fig. 2. Conserved binding mode of eight IMiDs in inducing neosubstrate ubiquitylation.**

(**A**) A close-up view of the IMiD binding region and substrate ubiquitylation region in eight IMiD-organized ubiquitylation assemblies.

(**B**) Guide to viewing the IMiD binding regions and substrate ubiquitylation regions shown in **C**.

(**C**) Close-up views showing the binding mode of eight IMiDs.

(**D**) Cartoon diagram illustrating the pathway for IMiD-organized complex assembly and summary of reported PDB structures of binary or ternary complexes containing eight IMiDs studied here.

(**E**) Structural alignments of individual IMiD-organized binary complex (colored white), ternary complex (colored gray), and ubiquitylation assembly (colored as **Fig. 1A** indicates), highlighting the conformational changes of CRBN TBD and Lon domains.

# Figure 3

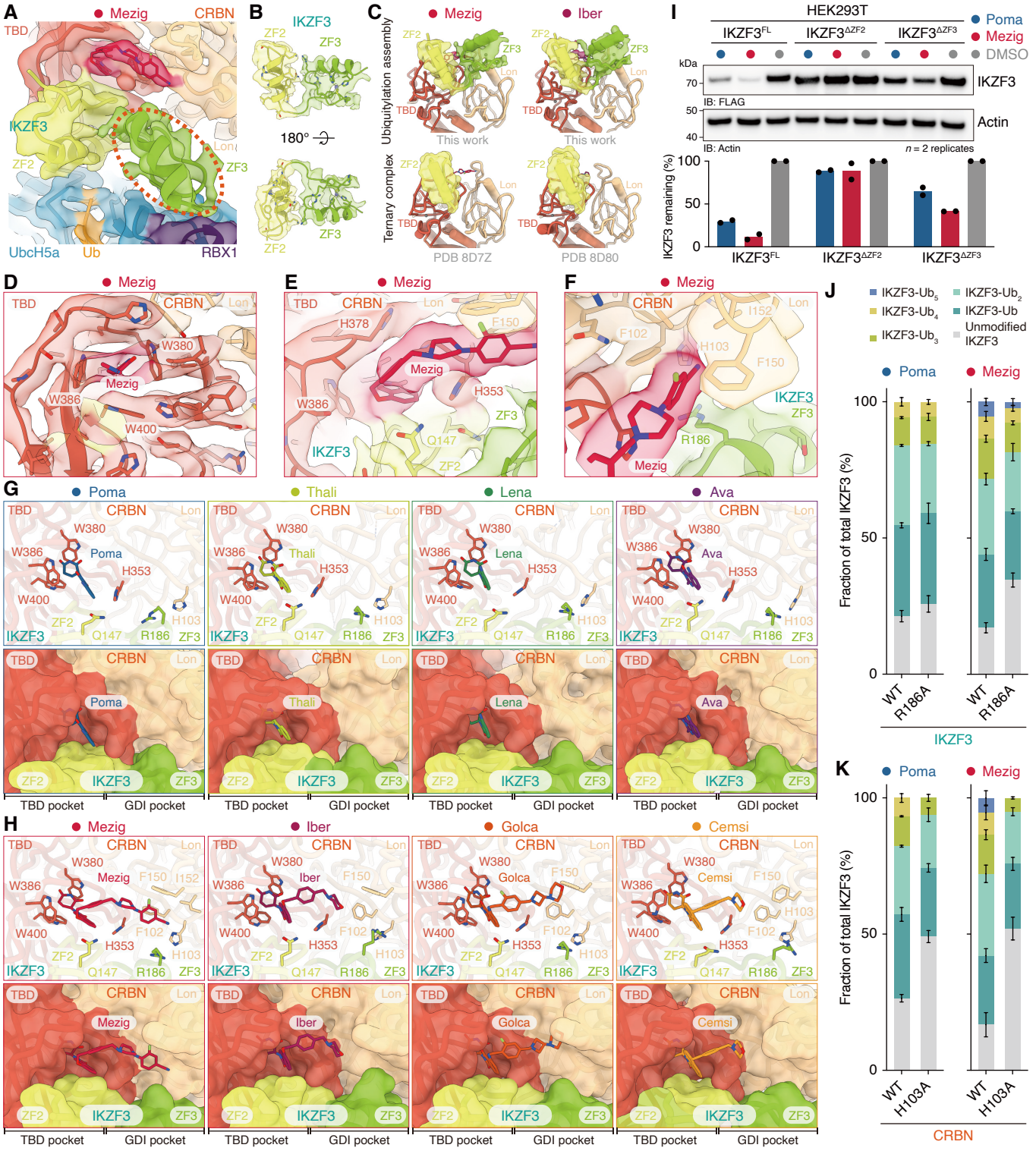

A
Mezig
CRBN
TBD
IKZF3
ZF2
ZF3
Lon
UbcH5a
Ub
RBX1
B
IKZF3
ZF2
ZF3
180°
C
Mezig
Iber
Ubiquitylation assembly
Ternary complex
This work
PDB 8D7Z
PDB 8D80
I
HEK293T
IKZF3FL
IKZF3ΔZF2
IKZF3ΔZF3
Poma
Mezig
DMSO
kDa
IKZF3
IB: FLAG
Actin
IB: Actin
n = 2 replicates
IKZF3 remaining (%)
D
E
F
W380
W386
W400
H378
F150
H353
Q147
I152
F102
H103
R186
G
Poma
Thali
Lena
Ava
TBD pocket
GDI pocket
H
Iber
Golca
Cemsi
J
IKZF3-Ub5
IKZF3-Ub2
IKZF3-Ub4
IKZF3-Ub
IKZF3-Ub3
Unmodified IKZF3
Fraction of total IKZF3 (%)
WT
R186A
IKZF3
K
H103A
CRBN

**Fig. 3. A cryptic GDI pocket formed by the IKZF3 non-degron motif ZF3 and CRBN Lon domain contributes to IMiD-induced IKZF3 ubiquitylation and degradation.**

(**A**) A close-up view of the Mezig structure with a cartoon model fit into the cryo-EM map. The red dashed circle indicates the unexpected IKZF3 ZF3 density.

(**B**) Two orientations of the IKZF3 cryo-EM density in the Mezig structure with cartoon model fit.

(**C**) Comparison of tandem ZF2–ZF3 motifs observed in mezigdomide- or iberdomide-organized ubiquitylation assemblies (top, this work) and ternary complexes (PDB 8D7Z, 8D80), revealing the absence of ZF3 density in ternary complexes. The ZF2–ZF3 motifs in ubiquitylation assemblies are shown as semi-transparent cryo-EM densities with cartoon model fit. The ZF2 motifs in ternary complexes (PDB 8D7Z, 8D80) are shown as semi-transparent cartoon surfaces and models.

(**D**) Detailed view of mezigdomide binding in the CRBN TBD pocket. Key TBD pocket residues, CRBN W380, W386, and W400, are indicated.

(**E**) Detailed view of mezigdomide interacting with CRBN and IKZF3. Key interacting residues, CRBN F150, H353, H378, W386, and IKZF3 Q147 are indicated.

(**F**) Detailed view of mezigdomide interacting with the IKZF3–CRBN GDI pocket. Key interacting residues, CRBN F102, H103, F150, I152, and IKZF3 R186, are indicated. Cryo-EM density map and atomic model are shown.

(**G**, **H**) Zoomed-in views of each IMiD molecule binding in the CRBN TBD pocket or GDI pocket. Side chains of key interacting amino acid residues are shown as stick models (top). Surface representations of CRBN and IKZF3 are used to highlight the structural features of the binding pockets.

(**I**) A representative western blot image (top) of *in vivo* degradation assay using $IKZF3^{FL}$, $IKZF3^{\Delta ZF2}$, or $IKZF3^{\Delta ZF3}$ construct and bar graph showing quantified IKZF3 degradation data from $n = 2$ technical replicates (bottom).

(**J**) *In vitro* ubiquitylation assay using WT IKZF3 ZF2–ZF3 or its R186A mutant in the presence of pomalidomide or mezigdomide.

(**K**) *In vitro* ubiquitylation assay using WT CRBN or its H103 mutant with the fully-assembled $_{N8}CRL4^{CRBN}$ E3 ligase complex. Bar graph comparing the fraction of unmodified and ubiquitylated IKZF3 species in the presence of eight IMiDs. Data are presented as mean ± SD from $n = 3$ technical replicates.

# Figure 4

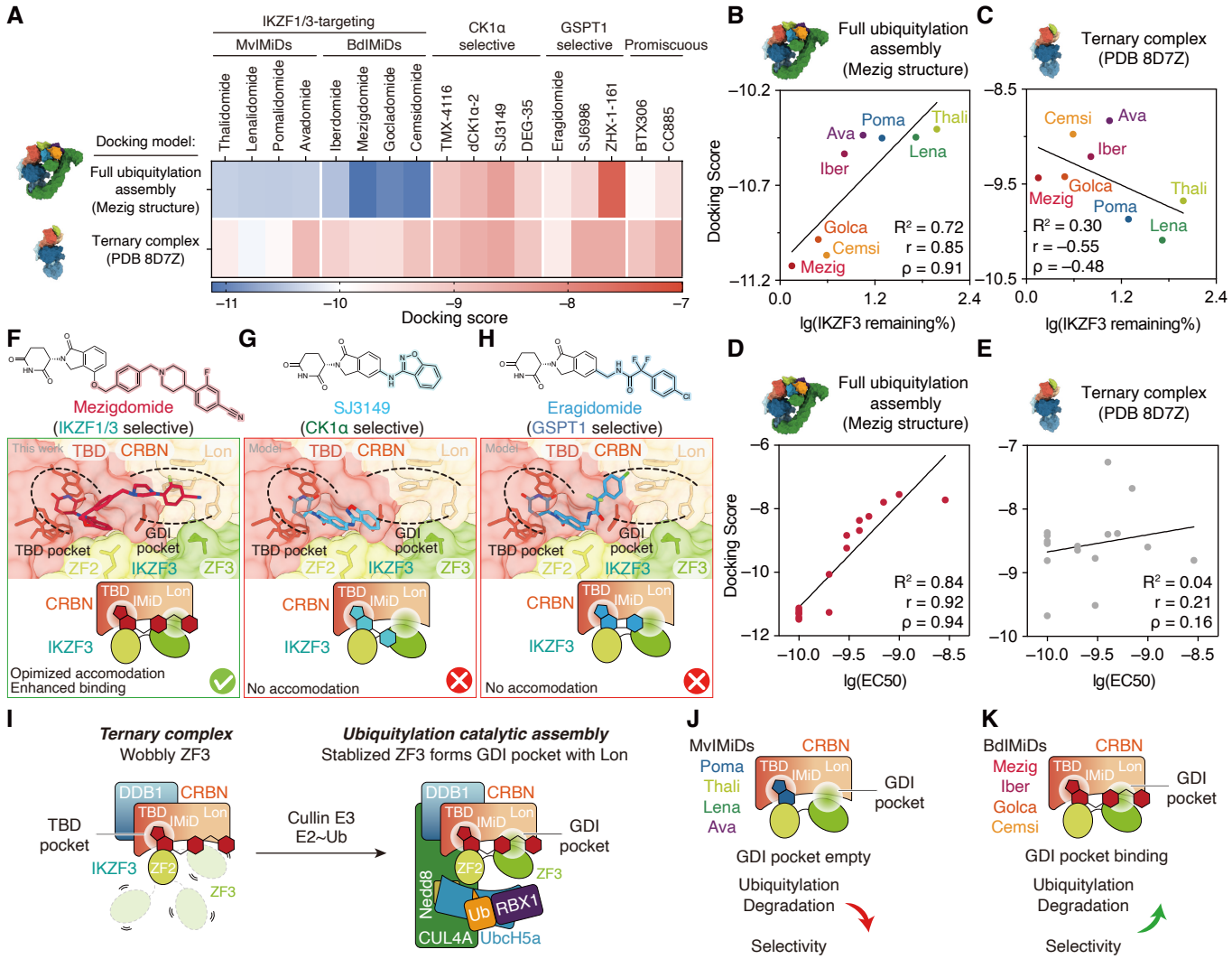
A
IKZF1/3-targeting
MvIMiDs
BdIMiDs
CK1α selective
GSPT1 selective
Promiscuous
Thalidomide
Lenalidomide
Pomalidomide
Avadomide
Iberdomide
Mezigdomide
Gocladomide
Cemsidomide
TMX-4116
dCK1α-2
SJ3149
DEG-35
Eragidomide
SJ6986
ZHX-1-161
BTX306
CC885
Docking model:
Full ubiquitylation assembly (Mezig structure)
Ternary complex (PDB 8D7Z)
−11
−10
−9
−8
−7
Docking score
B
Full ubiquitylation assembly (Mezig structure)
Docking Score
lg(IKZF3 remaining%)
Poma
Thali
Ava
Lena
Iber
Golca
Cemsi
Mezig
R² = 0.72
r = 0.85
ρ = 0.91
C
Ternary complex (PDB 8D7Z)
Cemsi
Ava
Iber
Golca
Mezig
Poma
Thali
Lena
R² = 0.30
r = −0.55
ρ = −0.48
D
Full ubiquitylation assembly (Mezig structure)
Docking Score
lg(EC50)
R² = 0.84
r = 0.92
ρ = 0.94
E
Ternary complex (PDB 8D7Z)
lg(EC50)
R² = 0.04
r = 0.21
ρ = 0.16
F
Mezigdomide
(IKZF1/3 selective)
G
SJ3149
(CK1α selective)
H
Eragidomide
(GSPT1 selective)
This work
Model
TBD
CRBN
Lon
TBD pocket
GDI pocket
ZF2
IKZF3
ZF3
IMiD
Opimized accomodation
Enhanced binding
No accomodation
I
Ternary complex
Wobbly ZF3
Ubiquitylation catalytic assembly
Stablized ZF3 forms GDI pocket with Lon
DDB1
Cullin E3
E2~Ub
Nedd8
Ub
RBX1
CUL4A
UbcH5a
J
MvIMiDs
Poma
Thali
Lena
Ava
GDI pocket
GDI pocket empty
Ubiquitylation
Degradation
Selectivity
K
BdIMiDs
Mezig
Iber
Golca
Cemsi
GDI pocket binding
Ubiquitylation
Degradation
Selectivity

**Fig. 4. The IMiD–GDI pocket interplay in the substrate ubiquitylation process provides a rational understanding of IMiDs' efficacy.**

(**A**) Heat map graphs showing docking scores of IMiDs with distinct target selectivities. Mezigdomide-organized full ubiquitylation assembly (Mezig complex) or ternary complex (PDB 8D7Z) was used as the docking model. Low (favorable) and high (unfavorable) docking scores are indicated by blue and red colors.

(**B**, **C**) Dot plots showing the correlation analysis of the logarithm of IKZF3 degradation potency [lg(IKZF3 remaining%)] for the eight IKZF3-targeting IMiDs against their docking scores within the full ubiquitylation complex (**B**) or ternary complex (**C**). IKZF3 degradation potency data are from **fig. S1B**.

(**D**, **E**) Dot plots showing the correlation analysis of the logarithm of previously reported IKZF3 EC50 [lg(EC50)] for mezigdomide analogs against their docking scores within the full ubiquitylation complex (**D**) or ternary complex (**E**). $R^2$ of the simple linear regression model, Pearson's correlation coefficient (r), and Spearman's correlation coefficient (ρ) are indicated.

(**F**) Structural analysis and schematic illustration of mezigdomide engaging both the CRBN TBD and GDI pockets in our cryo-EM structure of full ubiquitylation assembly.

(**G**, **H**) Structural analysis and schematic illustration of GSPT1-selective eragidomide (**G**) or CK1α-selective SJ3149 (**H**) docked into our Meizg structure.

(**I**) Cartoon diagram illustrating the pathway for the IMiD-organized ternary complex to catalytically active ubiquitylation assembly. Engagement of the fully-assembled $_{N8}CRL4^{CRBN}$ E3 ligase and E2~Ub enables the wobbly IKZF3 ZF3 motif to form the GDI pocket.

(**J**, **K**) Cartoon summary illustrating the rationale for understanding the molecular origin of the efficacy of MvIMiDs (**J**) or BdIMiDs (**K**) through IMiD–GDI pocket interplay.

Science
AAAS

# Supplementary Materials for

## A Cryptic Interfacial Pocket Uncovered in Full CRL4$^{CRBN}$ Ubiquitylation Complex Enhances IMiD Efficacy

Zhiheng Deng[1]†, Huasong Ai[2]†*, Qiang Shi[1]†, Jiawei Liang[1], Zaozhen He[1], Jiqing Zheng[1], Haoxiang Li[1], Liying Zhang[1], Wei He[1], Shixian Tao[1], Qingyun Zheng[2], Wei He[3], Man Pan[2]*, Lei Liu[1]*

Corresponding author: huasongai@sjtu.edu.cn (H.A.); panman@sjtu.edu.cn (M.P.); lliu@mail.tsinghua.edu.cn (L.L.)

**The PDF file includes:**

Materials and Methods
Figs. S1 to S12
Tables S1 to S3
References

**Other Supplementary Materials for this manuscript include the following:**

Data S1 to S3

## Materials and Methods

Cloning and plasmid construction

The cDNA of human CUL4A (Uniprot entry Q13619, full length, amino acid residues 1–759), RBX1 (Uniprot entry P62877, full length, amino acid residues 1–108), Nedd8 (Uniprot entry Q15843, full length, amino acid residues 1–81), UbcH5a (Uniprot entry P51668, full length, amino acid residues 1–147), and IKZF3 (Uniprot entry Q9UKT9, tandem ZF2–ZF3, amino acid residues 142–198) were synthesized with sequence optimization for *Escherichia coli* recombinant expression by GenScript Biotech (Nanjing, China). The cDNA of human DDB1 (Uniprot entry Q16531, full length, amino acid residues 1–1,140), CRBN (Uniprot entry Q96SW2, amino acid residues 40–442) were synthesized with sequence optimization for HEK293F overexpression by GenScript Biotech (Nanjing, China).

RBX1 and CUL4A were cloned into our home-modified pET29a-YS14 polycistronic vector (*1*) with an N-terminal $His_6$–HRV3C-tag and an N-terminal MysB–HRV3C–StrepII-tag, respectively, according to a reported strategy (*2*). Nedd8 was cloned into a pET22b vector without any tag. UbcH5a or IKZF3 tandem ZF2–ZF3 was individually cloned into a pET28a vector with an N-terminal $His_6$–HRV3C-tag or N-terminal MBP–HRV3C–HA-tag, respectively. DDB1 or CRBN was individually cloned into our home-modified pGX033 vector (pcDNA3.1 backbone with EF1a promoter and WPRE element) (*1*) with an N-terminal FLAG-tag or $His_8$–HRV3C-tag, respectively. The Nedd8 E1 enzyme complex NAE1/UBA3 was cloned into a pGEX-6P-1 vector with an N-terminal GST-tag on NAE1 for polycistronic expression. The Nedd8 E2 enzyme UBE2M was cloned into a pGEX-6P-1 vector with an N-terminal GST-tag. Mutations or truncations were introduced by standard site-directed PCR mutagenesis or homologous recombination.

Protein expression and purification

The RBX1/CUL4A complex was polycistronically expressed and purified through a two-step affinity chromatography process. Plasmids containing RBX1/CUL4A were transformed into *Escherichia coli* BL21(DE3) cells (Transgene). Cells were cultured at 37 °C in Luria–Bertani (LB) medium supplemented with 50 μg $mL^{-1}$ kanamycin until reaching an optical density at 600 nm ($OD_{600}$) of 0.8, then induced overnight at 16 °C with 0.2 μM $ZnCl_2$ and 0.5 mM isopropyl β-D-thiogalactopyranoside (IPTG). After centrifugation, cells were lysed by sonication in ice-cold CRL lysis buffer containing 50 mM Tris-HCl (pH 7.5), 300 mM NaCl, 20 mM imidazole, 10% (v/v) glycerol, and 1 mM phenylmethylsulfonyl fluoride (PMSF). Cell lysates were clarified by centrifugation at 12,000 rpm for 30 min at 4 °C, and the supernatant was subsequently loaded onto a Ni-NTA affinity chromatography column. The $His_6$–HRV3C–RBX1/MysB–HRV3C–StrepII–CUL4A protein complex was eluted using Ni elution buffer (50 mM Tris-HCl, pH 7.5, 300 mM NaCl, 300 mM imidazole, and 10% (v/v) glycerol). The eluted proteins were then dialyzed overnight at 4 °C against a buffer containing 50 mM Tris-HCl (pH 7.5), 50 mM NaCl, 5% (v/v) glycerol, and 1 mM dithiothreitol (DTT), during which the $His_6$-tags on RBX1 and MysB-tags on CUL4A were removed by the addition of HRV3C protease. Dialysed proteins were incubated with streptactin resins (Smart-Lifesciences) for 2 h at 4 °C. After extensive wash, RBX1/StrepII–CUL4A complexes were eluted with buffer containing 50 mM Tris-HCl (pH 7.5), 50 mM NaCl, 5% (v/v) glycerol, 1 mM DTT, and 2.5 mM D-desthiobiotin (IBA Lifesciences). The RBX1/StrepII-CUL4A complex was further purified using a Superdex 200 10/300 GL size-exclusion column (GE Healthcare) pre-equilibrated in CRL SEC buffer (20 mM HEPES, pH 7.5, 150 mM NaCl, 2% (v/v) glycerol, 1 mM DTT).

The DDB1/CRBN complex and its mutants were expressed in mammalian cells. HEK293F cells were cultured in Union-293 chemically defined medium (Union-Biotech) to a density of approximately $1.5\times10^6$ cells $mL^{-1}$. DDB1 and CRBN plasmids were transiently co-transfected using polyethyleneimine (PEI, Polysciences). A total of 1.5 mg plasmids and 4.5 mg PEI were mixed in 50 mL of fresh medium for 15–20 min and then added to 1 L of cell culture. After 60 hours of incubation at 37 °C in a shaker with 5% $CO_2$, the transfected cells were collected by centrifugation. The resulting cell pellets were lysed by sonication following resuspension in ice-cold 293F lysis buffer (25 mM HEPES, pH 8.0, 200 mM KCl, 10% (v/v) glycerol, 0.01% (v/v) Triton X-100) supplemented with EDTA-free protease inhibitor tablets (Roche, cOmplete tablets). Cellular debris was cleared by centrifugation at 20,000 × g for 45 min at 4 °C, and the resulting supernatant was incubated with anti-FLAG affinity resin for 2 h at 4 °C. The bound DDB1/CRBN complex was eluted using 293F lysis buffer supplemented with 0.75 mg $mL^{-1}$ FLAG peptide. The DDB1/CRBN complex was subsequently purified by size-exclusion chromatography using either a Superdex 200 10/300 GL size-exclusion column (GE Healthcare) pre-equilibrated with buffer containing 25 mM HEPES (pH 7.5), 200 mM KCl, and 1 mM DTT.

Nedd8 was expressed in *Escherichia coli* Rosetta(DE3) cells (Solarbio). The cells were grown in LB medium supplemented with 50 μg $mL^{-1}$ ampicillin at 37 °C until reaching an $OD_{600}$ of 1.0, and protein expression was induced by adding 0.6 mM IPTG, followed by overnight incubation at 18 °C. Cells were harvested by centrifugation and lysed via sonication in N8 lysis buffer (50 mM HEPES, pH 7.5, 150 mM NaCl). The lysate was subjected to ultracentrifugation at 12,000 rpm for 30 min at 4 °C. The resulting pellet was resuspended in unfolding buffer (20 mM Tris-HCl, pH 7.8, 6 M guanidine hydrochloride (Gn-HCl), 1 mM DTT), and a second round of ultracentrifugation was performed. The supernatant was dialyzed overnight against double-distilled water ($ddH_2O$) containing 0.1% (v/v) trifluoroacetic acid (TFA). After dialysis, the mixture was clarified again by ultracentrifugation, and the resulting supernatant was purified by semi-preparative reverse-phase high-performance liquid chromatography (RP-HPLC), followed by electrospray ionization mass spectrometry (ESI-MS) characterization. The purified Nedd8 protein was then lyophilized into powder. For refolding, the lyophilized Nedd8 protein was first dissolved in unfolding buffer and then gradually diluted by adding N8 lysis buffer. Final purification was carried out using a Superdex 75 Increase 10/300 GL column (GE Healthcare) pre-equilibrated with N8 lysis buffer.

IKZF3 tandem ZF2–ZF3 motif and its mutants were expressed in *Escherichia coli* BL21(DE3) cells (Transgene). Cell cultures were grown at 37 °C in LB medium supplemented with 50 μg $mL^{-1}$ kanamycin until the $OD_{600}$ reached 1.0. IKZF3 expression was then induced by adding 0.2 μM $ZnCl_2$ and 0.5 mM IPTG, followed by overnight incubation at 16 °C. Cells were harvested by centrifugation and lysed by sonication in ice-cold IKZF lysis buffer composed of 50 mM Tris-HCl (pH 7.5), 200 mM NaCl, 10% (v/v) glycerol, 1 mM DTT, 50 μM $ZnCl_2$, and 1 mM PMSF. After centrifugation, the clarified supernatant was applied to an MBP-Tag Dextrin Resin (PurKine™, Abbkine) for 4 h at 4 °C. After extensive wash by IKZF wash buffer (50 mM Tris-HCl, pH 7.5, 200 mM NaCl, 10% (v/v) glycerol, 1 mM DTT, and 50 μM $ZnCl_2$), HRV3C protease was introduced into the resin suspension in IKZF wash buffer and incubated under gentle agitation overnight at 4 °C to cleave IKZF3 ZF2–ZF3 proteins from the resin. Cleaved IKZF3 ZF2–ZF3 proteins were further purified using a Superdex 75 Increase 10/300 GL column (GE Healthcare) pre-equilibrated with CRL SEC buffer.

UbcH5a was expressed in *Escherichia coli* BL21(DE3) cells (Transgene) and purified by Ni affinity chromatography, HRV3C protease cleavage, and size-exclusion chromatography (Superdex 75 10/300 GL column, GE Healthcare).

NAE1/UBA3 and UBE2M were individually expressed and purified from *Escherichia coli* BL21(DE3) cells (Transgene). For NAE1/UBA3, the cells were cultured in LB medium supplemented with 50 μg $mL^{-1}$ ampicillin at 37 °C to an $OD_{600}$ of 1.0 and induced by the addition of 0.4 mM IPTG at 16 °C overnight. Cells were harvested by centrifugation and lysed by sonication in GST lysis buffer (25 mM HEPES, pH 7.5, 150 mM NaCl, 10% (v/v) glycerol, 1 mM DTT). Lysates were ultracentrifuged at 12,000 rpm for 30 min at 4 °C, and the resulting supernatant was loaded onto a Glutathione Beads 4FF (Lableads). The NAE1/UBA3 proteins were eluted using GST lysis buffer supplemented with 30 mM reduced glutathione (GSH), followed by HRV3C protease cleavage overnight. The protein was further purified by ion exchange chromatography using a 5 mL HiTrap Q column. The UBE2M protein was expressed and purified following the same procedure as NAE1/UBA3, with the exception that the final purification step was performed using a Hiload 16/600 SD75 pg column (GE Healthcare) pre-equilibrated with a buffer containing 50 mM HEPES (pH 7.5 and 150 mM NaCl.

Ubiquitin (Ub) and its mutants were expressed and purified as previously described(*3*). Briefly, proteins were overexpressed in *Escherichia coli* BL21(DE3) cells (Transgene). Following cell harvest, pellets were resuspended in $ddH_2O$ and lysed by sonication. The lysates were treated with 1% (v/v) perchloric acid to precipitate contaminants and subsequently clarified by centrifugation. The resulting supernatant was dialysed against $ddH_2O$ containing 0.1% (v/v) TFA overnight and then purified using a Source15S cation exchange column (GE Healthcare). Fractions corresponding to Ub were pooled and dialyzed against a buffer containing 20 mM HEPES (pH 7.5) and 150 mM NaCl.

Reconstitution of $_{N8}CRL4^{CRBN}$ E3 ligase complex

For neddylation of RBX1/CUL4A, 0.8 μM NAE1/UBA3, 6.5 μM UBE2M, 20 μM Nedd8, and 2.5 μM RBX1/CUL4A were mixed in a buffer containing 50 mM Tris-HCl (pH 7.5), 150 mM NaCl, 1 mM DTT, 5 mM adenosine 5'-phosphate (ATP), and 5 mM $MgCl_2$. The reaction mixture was incubated at 27 °C for 4 h. Following confirmation of complete neddylation of CUL4A by SDS–PAGE analysis, the DDB1/CRBN complex was subsequently added to the reaction mixture at a molar ratio corresponding to 0.75 equivalents relative to RBX1/CUL4A. The mixture was incubated at 4 °C for 2 h and purified by a Superdex 200 10/300 GL column (GE Healthcare) pre-equilibrated with CRL SEC buffer. Fractions containing the $_{N8}CRL4^{CRBN}$ E3 ligase complex were pooled, analyzed by SDS–PAGE, concentrated to ~2.6 mg $mL^{-1}$, and stored at –80 °C.

Fluorescent labeling of ubiquitin

Ub-MCQ (a ubiquitin variant with an additional cysteine inserted following the N-terminal methionine) was concentrated to approximately 20 mg $mL^{-1}$ in buffer containing 20 mM HEPES (pH 7.5) and 150 mM NaCl. Oregon Green™ 488 (OG488) maleimide (1.2 equivalents, prepared as a 20 mg $mL^{-1}$ stock in dimethyl sulfoxide (DMSO), purchased from Thermo Fisher Scientific) was then added, and the pH of the solution was adjusted to 7.4. The reaction was carried out at 4 °C for 24 h and subsequently quenched by the addition of DTT to a final concentration of 100 mM. The fluorescently labeled ubiquitin ($Ub^{OG488}$) was purified via size-exclusion chromatography using a Superdex 75 column (GE Healthcare) pre-equilibrated with a buffer containing 20 mM HEPES (pH 7.5), 150 mM NaCl, 2% (v/v) glycerol, and 1 mM DTT.

Chemical synthesis of IKZF3–Ub ABP

The IKZF3–Ub ABP was synthesized following previously reported protocols (*4, 5*) with some modifications (fig. S2B). Initially, lyophilized Ub(1–75)-MesNa (3 mg $mL^{-1}$, prepared following the described protocol (*6*)) was dissolved in reaction buffer (20 mM HEPES, pH 7.5, 6 M Gn-HCl). Subsequently, 400 mM (E)-3-[2-(bromomethyl)1,3-dioxolan-2-yl]prop-2-en-1-amine (BmDPA, Bide Pharmatech Co., Ltd) was added to the solution without adjusting the pH. The reaction mixture was incubated in the dark at 37 °C for 2 h, followed by purification via semi-preparative RP-HPLC and characterization by ESI-MS. The purified product was lyophilized and dissolved at a concentration of 0.5 mg $mL^{-1}$ in deprotection buffer (20 mM HEPES, 6 M Gn-HCl, 54% (v/v) TFA, 40 mM p-toluenesulfonic acid). Deprotection was performed in the dark at 37 °C for 1 h. The resulting Ub–BmDPA was then purified by semi-preparative RP-HPLC, confirmed by ESI-MS analysis (fig. S2C), and lyophilized into powder.

Lyophilized Ub–BmDPA was dissolved in a buffer containing 100 mM $NaH_2PO_4$ (pH 6.0), 8 M urea, and 500 mM NaCl to prepare a solution at a final concentration of around 1 mg $mL^{-1}$. The Ub–BmDPA solution was then dialyzed against a buffer containing 100 mM $NaH_2PO_4$ (pH 6.0) and 100 mM NaCl overnight at 4 °C. The dialyzed sample containing refolded Ub–BmDPA was pooled and concentrated to ~10 mg $mL^{-1}$.

The IKZF3 ZF2–ZF3 sequence contains a non-zinc-coordinating cysteine residue at position 183 (C183). To ensure site-specific reactivity at the K166C position, C183 was mutated to threonine (C183T). Purified IKZF3 ZF2–ZF3 C183T/K166C proteins (at a final concentration of 300 μM) were mixed with Ub–BmDPA (0.75 equivalents to IKZF3 ZF2–ZF3 C183T/K166C) to initiate the nucleophilic substitution reaction. The reaction mixture was incubated at 30 °C for 15 min, and then immediately loaded onto a Superdex 75 Increase column (GE Healthcare) pre-equilibrated with a buffer containing 20 mM HEPES (pH 7.5), 150 mM NaCl, 2% (v/v) glycerol. Fractions containing IKZF3–Ub ABP were pooled, analyzed by SDS–PAGE (fig. S2D), concentrated to 0.5 mg $mL^{-1}$, and stored at –80 °C.

IMiD chemicals

Eight IKZF1/3-targeting IMiD molecules used in this study were purchased from commercial suppliers and used without further purification. Pomalidomide (CC-4047, Cat# HY-111109) and lenalidomide (CC-5013, Cat# HY-A0003) were purchased from MedChemExpress. Thalidomide (Cat# S1193), avadomide (CC-122, Cat# S7892), iberdomide (CC-220, Cat# S8760), mezigdomide (CC-92480, Cat# S8975), golcadomide (CC-99282, Cat# E1212), and cemsidomide (CFT7455, Cat# E1184) were purchased from Selleck. The IMiD chemicals were supplied as dry powders and individually dissolved in anhydrous DMSO to prepare 10 mM stock solutions. Aliquots were stored at –80 °C for future use.

*In vitro* ubiquitylation assays

Generally, assays were conducted in a reaction mixture containing human UBA1, UbcH5a, $_{N8}CRL4^{CRBN}$ E3 ligase complex, IKZF3 tandem ZF2–ZF3 motifs, $Ub^{OG488}$, and IMiDs in Ub assay buffer (50 mM Tris-HCl, pH 7.5, 150 mM NaCl, 10 μM $ZnCl_2$, 2 mM $MgCl_2$, 3 mM ATP, and 1 mM DTT). In all experiments, the final concentration of DMSO introduced by the IMiD stock solution was maintained at 2% (v/v) in the reaction mixture. Before use, all enzymes — including relevant fragments and mutants — were analyzed by SDS–PAGE (SurePAGE gels, GenScript Biotech) (Data S3). Reactions were terminated by the addition of 4 × LDS loading buffer (Thermo Fisher Scientific) supplemented with 100 mM DTT, followed by heating at 95 °C for 5 min.

Reactions were then resolved by SDS–PAGE (NuPAGE gels, Thermo Fisher Scientific). Uncropped gel images are provided in Data S2.

UBA1, UbcH5a, $_{N8}$CRL4$^{CRBN}$ E3 ligase complex, IMiD, and IKZF3 ZF2–ZF3 were first mixed in Ub assay buffer and incubated on ice for 5 min. Then Ub$^{OG488}$ was introduced into the mixture to initiate ubiquitylation reactions.

For the IKZF3 and CRBN mutagenesis assays shown in Figs. 3J and 3K, 1.0 μM UBA1, 2.0 μM UbcH5a, 0.10 μM $_{N8}$CRL4$^{CRBN}$ E3 ligase complex or its CRBN H103A mutant, 5.0 μM IKZF3 ZF2–ZF3 or its R186A mutant, 10.0 μM Ub$^{OG488}$, and 2.0 μM IMiD were used. Reactions were incubated at 37 °C and quenched at $t$ = 10 min. Samples were resolved on 12% NuPAGE Bis-Tris gels (Thermo Fisher Scientific).

Experiments were performed in technical triplicate ($n$ = 3).

*In vivo* degradation assays

HEK293T cells were maintained in Dulbecco's modified Eagle's medium (DMEM, Thermo Fisher Scientific) supplemented with 10% (v/v) fetal bovine serum (FBS, Thermo Fisher Scientific) and 0.01% (v/v) penicillin-streptomycin stock (10,000 U mL$^{-1}$, Thermo Fisher Scientific). HEK293T cells plated in 6-well plates were transfected with pcDNA3.1 plasmids (2.5 μg per well) containing N-terminal FLAG-tagged full-length IKZF3 (IKZF3$^{FL}$) or zinc finger deletion constructs (IKZF3$^{\Delta ZF2}$ or IKZF3$^{\Delta ZF3}$) using Lipofectamine 3000 reagent (Thermo Fischer Scientific). After 24 h of transfection, the culture medium was replaced with fresh medium supplemented with individual IMiD at a final concentration of 5 μM for each compound. In all wells, the final concentration of DMSO was maintained at 0.005% (v/v) in the medium. After 48 h of IMiD treatment, cells were washed with ice-cold phosphate buffered saline (PBS, Thermo Fischer Scientific) and harvested using cell scrapers. Harvested cells were pelleted by centrifugation. Cells were processed using Minute Total Protein Extraction Kit for Animal Cultured Cells and Tissues (Cat# SD-001/SN-002, Invent Biotechnologies, Inc.) following the protocol provided by the supplier to prepare the cell lysates. Total proteins in cell lysates were immediately measured using Pierce BCA Protein Assay Kits (Thermo Fischer Scientific) and analyzed by western blots as previously described (*1*). Briefly, following the membrane transfer procedure, the polyvinylidene difluoride (PVDF) membrane (Immobilon-P, Merck Millipore) was horizontally cut at the 50 kDa molecular weight marker. After blocking, the upper portion (> 50 kDa) was probed with a rabbit monoclonal anti-FLAG antibody (Cell Signaling Technology, Cat# D6W5B, 1:1,000 diluted), while the lower portion (< 50 kDa) was probed with a rabbit monoclonal anti-β-actin antibody (Cell Signaling Technology, Cat# 4970S, 1:4,000 diluted). An HRP-conjugated goat-anti-rabbit IgG antibody (2031, Huaxingbio) was used as the secondary antibody. The membranes were visualized using the Clarity Western ECL substrate (Bio-Rad) and imaged with a ChemiDoc MP Imaging System (Bio-Rad). Experiments were performed in technical duplicate ($n$ = 2). Uncropped blot images are provided in Data S2.

Cryo-EM sample preparation

UbcH5a protein was reduced by 1 mM TCEP for 30 min on ice, and desalted into a buffer containing 20 mM HEPES (pH 7.5), 150 mM NaCl using a Zeba desalting column (Thermo Fisher Scientific). Next, desalted UbcH5a IAD protein (9.8 μM, final concentration) was immediately added to the reaction mixture that contained $_{N8}$CRL4$^{CRBN}$ E3 ligase complex (3.2 μM, final concentration), IKZF3–Ub ABP (48 μM, final concentration), and IMiD reagent (15 μM, final concentration). In all reaction mixtures, the final concentration of DMSO was maintained under

0.3% (v/v). The chemical trapping reactions were incubated for 60 min at 30 °C and analyzed by SDS–PAGE. The trapped ubiquitylation assembly complexes were purified using a Superdex 200 Increase 5/150 GL column or a Superose 6 Increase 5/150 GL column (GE Healthcare) pre-equilibrated with CRL REC buffer (20 mM HEPES, pH 7.5, 75 mM NaCl, 1 mM TCEP). Peak fractions were pooled, analyzed by SDS–PAGE, concentrated to 0.3–0.4 mg $mL^{-1}$, and immediately subjected to cryo-EM sample preparation.

Just before grid preparation, lauryl maltose neopentyl glycol (LMNG, at a final concentration of 0.0025% (m/v)) was added to the sample to improve particle dispersity. A 3.5 µL aliquot of the sample was applied to glow-discharged holey gold grids (Quantifoil R1.2/1.3, Au 300 mesh) and incubated at 8 °C under 100% humidity for 60 seconds. The initial sample was removed from the grid using a pipette, followed by the application of a new 3.5 µL aliquot for an additional 60-second incubation. Grids were blotted and rapidly plunge-frozen in liquid ethane using a Vitrobot (Thermo Fisher Scientific).

Cryo-EM data collection

A total of 13,668 cryo-EM micrographs of the pomalidomide dataset were collected on a 300 kV Titan Krios microscope configured with a Gatan K3 direct electron detector camera (Tsinghua University, Branch of China National Center for Protein Sciences, Beijing) using the AutoEMation software (*7*). Micrographs of the pomalidomide dataset were recorded at a pixel size of 1.10 Å with a magnification of 81,000× and a dose of 50 $e^{-}$ $Å^{-2}$ for 32 frames with a defocus range of –1.0 to –1.8 µm. A total of 7,706 (the thalidomide dataset), 7,621 (the lenalidomide dataset), 8,474 (the avadomide dataset), 8,097 (the iberdomide dataset), 25,882 (the mezigdomide dataset), 8,567 (the golcadomide dataset), and 7,205 (the cemsidomide dataset) cryo-EM micrographs were collected on a 300 kV Titan Krios G4 microscope configured with a Falcon4 direct electron detector camera (Shuimu BioSciences, Hangzhou) using the EPU software (Thermo Fisher Scientific). For the mezigdomide dataset, micrographs were collected at a magnification of 96,000× with a pixel size of 0.830 Å. A total electron dose of 50 $e^{-}$ $Å^{-2}$ was applied over 32 frames, with a defocus range of –1.2 to –2.0 µm. Micrographs for the remaining six datasets (the thalidomide, lenalidomide, avadomide, iberdomide, golcadomide, and cemsidomide datasets) were acquired at 75,000× magnification, corresponding to a pixel size of 1.059 Å, under identical exposure conditions.

Cryo-EM data processing

All datasets were processed using RELION v3.1.1 (*8*). Motion correction, contrast transfer function (CTF) estimation, manual or automated particle picking, and particle extraction were performed. Subsequent steps included iterative 2D and 3D classifications, mask generation, 3D auto-refinement, and postprocessing. Data processing flow charts are detailed in fig. S3 (the mezigdomide dataset) and Data S1 (the thalidomide, lenalidomide, pomalidomide, avadomide, iberdomide, golcadomide, and cemsidomide datasets). To improve the cryo-EM density of IKZF ZF3, a mask and focused 3D classifications were applied to the CRBN TBD–Lon–IKZF3–UbcH5a–RBX1 region. Particles exhibiting the best ZF3 features were selected and used for the final reconstruction. Cryo-EM data processing statistics are summarized in Tables S1 and S2. Overall resolutions were determined based on the gold standard Fourier shell correlation (FSC) criterion at 0.143, and local resolution estimations were carried out using ResMap v1.1.4.

Model building, refinement, and validation

An initial model containing mezigdomide was generated using previously reported models of subunits or subcomplexes: the cullin scaffold containing CUL4A and Nedd8 and the catalytic module containing RBX1, UbcH5a, and Ub (PDB 8B3G) (*9*), the ternary module containing DDB1, CRBN, IKZF3, and mezigdomide (PDB 8D7Z) (*10*). The IKZF1 ZF2 motif in PDB entry 8D7Z was replaced with the AlphaFold2 (*11*) model of the IKZF3 ZF2 motif (Q9UKT9-F1-v4), and the IKZF3 ZF3 motif was further added based on the AlphaFold2 model. These models were manually fit into the mezigdomide cryo-EM map by rigid-body docking using UCSF ChimeraX v1.9 (*12*). The initial model was generated based on the coordinates manually docked in UCSF ChimeraX using COOT v0.8.2 (*13*). Next, one round of real-space refinement using Phenix v1.21.1 (*14*) was performed to yield an initial refined model. The mezigdomide molecule in the initially refined model was individually replaced with each of the other seven IMiDs. The restraints and coordinates of five IMiDs were derived from previously reported crystal structures of binary or ternary complexes: thalidomide (PDB 4CI1) (*15*), lenalidomide (PDB 4CI2) (*15*), pomalidomide (PDB 4CI3) (*15*), avadomide (PDB 7PSO) (*16*), and iberdomide (PDB 8D80) (*10*). As no binary/ternary structures containing golcadomide or cemsidomide had been reported when we conducted model building, restraints and initial PDB models for golcadomide and cemsidomide were generated using the eLBOW program in Phenix-1.21.1 (*14*). Iterative cycles of real-space refinement using Phenix v1.21.1 (*14*) and manual model adjustment with COOT v0.8.2 (*13*) were performed until satisfactory map-to-model correlation and geometry were obtained. Protein backbone segments and side chains not supported by cryo-EM density were manually removed. Tables S1 and S2 provide a summary of all statistics related to model building, refinement, and validations. All structural interpretations, visualizations were performed using UCSF ChimeraX v1.9 (*12*).

*In silico* docking

Molecular docking was performed following standard protocols using Maestro 14.1 (Schrödinger, New York). The mezigdomide-organized full ubiquitylation complex resolved in this study and previously reported IKZF1–mezigdomide–CRBN/DDB1 (PDB 8D7Z) ternary complex were prepared using the Protein Preparation programme. The receptor grid was centered on mezigdomide for grid generation. The LigPrep programme was employed to generate conformers of TMX-4116, dCK1α-2, SJ3149, DEG-35, eragidomide, SJ6986, ZHX-1-161, BTX306, CC-885 and mezigdomide analog molecules. Docking was carried out using the Glide module in standard precision mode. Docking results were evaluated based on the docking score and visualized in UCSF ChimeraX v1.9 (*12*).

Protein bands quantification and data analysis

For *in vitro* ubiquitylation assays, protein band quantification was performed as previously described (*1*). Gels were imaged using a ChemiDoc MP Imaging System (Bio-Rad). Initially, the Fluorescein setting was used to visualize fluorescent proteins, followed by the Coomassie Far Red Epi mode to detect protein ladders. The same gel was subsequently stained with Coomassie Brilliant Blue (CBB). Fluorescent and Coomassie Far Red Epi images were merged to estimate the molecular weights of the fluorescent proteins. Quantitative analysis of protein bands in both unmerged fluorescent gel images and CBB-stained gel images was carried out using Image Lab 6.0.1 (Bio-Rad). Boxes were drawn around the ubiquitylated and unmodified IKZF3 bands in the CBB-stained gel images, followed by background signal subtraction. Intensities of protein bands

in each lane were calculated. Fractions of total IKZF3 (%) were calculated by dividing the band intensity of the ubiquitylated IKZF3 species (e.g., IKZF3–Ub) by the total band intensity of all IKZF3 species in the same lane.

For *in vivo* degradation assays, boxes were placed around the IKZF3 bands and actin bands in the blot images, and background signals were subtracted. IKZF3 remaining (%) was calculated by dividing the band intensity of the IKZF3 band by the intensity actin band in the same lane.

# Figure S1

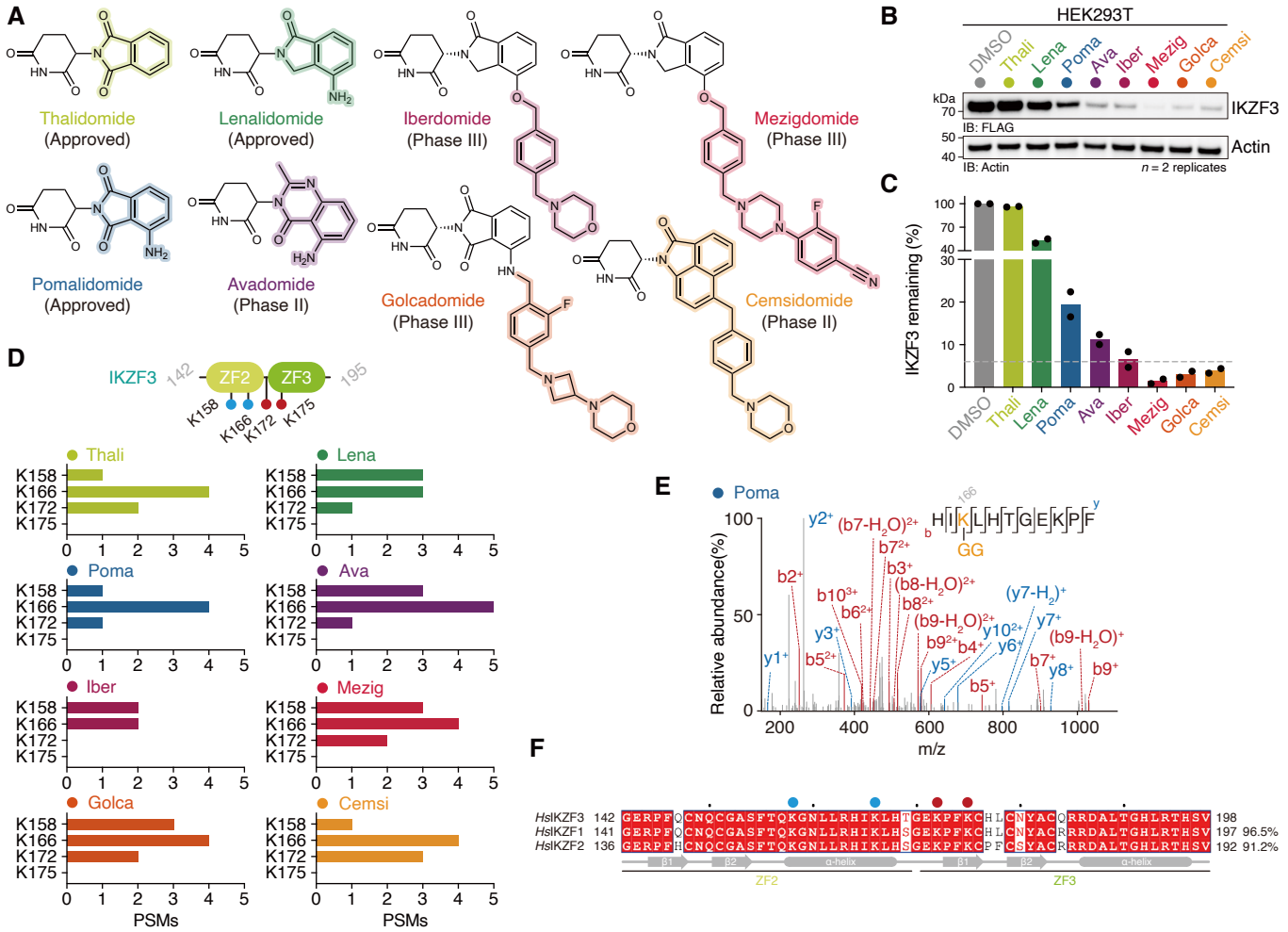
A
Thalidomide
(Approved)
Lenalidomide
(Approved)
Iberdomide
(Phase III)
Mezigdomide
(Phase III)
Pomalidomide
(Approved)
Avadomide
(Phase II)
Golcadomide
(Phase III)
Cemsidomide
(Phase II)
B
HEK293T
DMSO
Thali
Lena
Poma
Ava
Iber
Mezig
Golca
Cemsi
kDa
70
50
40
IKZF3
IB: FLAG
Actin
IB: Actin
n = 2 replicates
C
IKZF3 remaining (%)
100
70
40
30
20
10
0
D
IKZF3
142
ZF2
ZF3
195
K158
K166
K172
K175
Thali
Lena
Poma
Ava
Iber
Mezig
Golca
Cemsi
PSMs
E
Poma
Relative abundance(%)
m/z
GG
F
HsIKZF3 142 198
HsIKZF1 141 197 96.5%
HsIKZF2 136 192 91.2%
ZF2
ZF3

**Fig. S1. Approved and clinical IMiDs exhibit distinct degradation efficiencies and site-selective ubiquitylation of IKZF3.**

(**A**) Chemical structures of eight approved and clinical IKZF3-targeting IMiDs, with differences in each molecule highlighted by color.

(**B**) A representative western blot image of *in vivo* IKZF3 degradation assay in the presence of each IMiD (1 μM final concentration).

(**C**) Bar graph showing quantified IKZF3 degradation data from $n = 2$ technical replicates.

(**D**) Bar graphs showing the Peptide-Spectrum Matches (PSMs) of peptides containing lysine residues (K158, K166, K172, or K175) modified with GG remnant.

(**E**) A representative tandem mass spectrum (MS/MS spectrum) for a peptide containing a GG remnant modified on IKZF3 K166 derived from *in vitro* ubiquitylation assays using pomalidomide.

(**F**) Sequence alignment of tandem ZF2–ZF3 motifs in human Ikaros family transcription factors IKZF3, IKZF1, and IKZF2. Consensus lysines on the ZF2 or ZF3 motif are indicated by blue or red dots, respectively.

# Figure S2

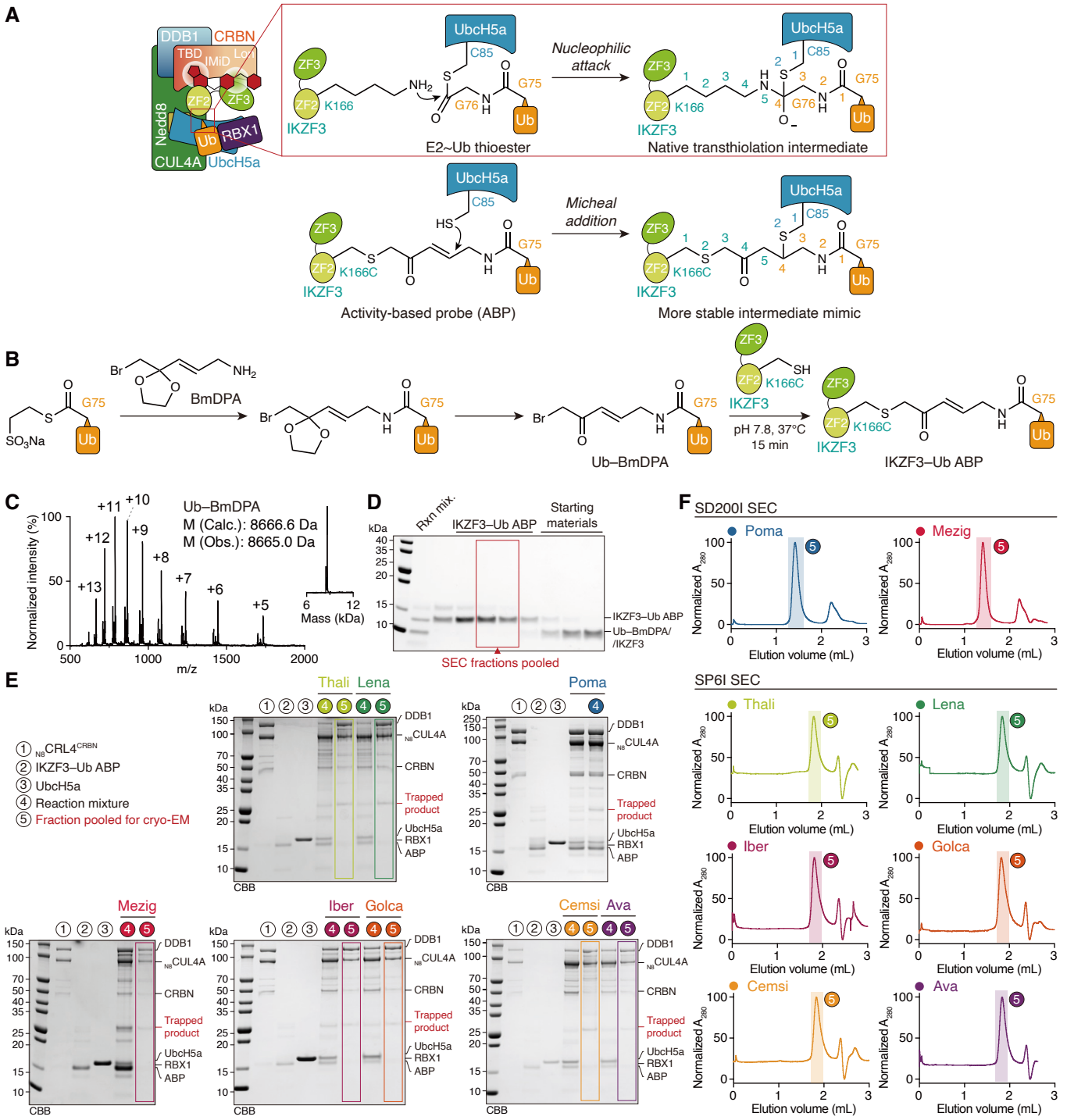
A
DDB1
CRBN
TBD
IMiD
Loop
ZF2
ZF3
Nedd8
Ub
RBX1
CUL4A
UbcH5a
UbcH5a
C85
ZF3
ZF2
K166
IKZF3
G75
G76
Ub
E2~Ub thioester
Nucleophilic attack
Native transthiolation intermediate
K166C
Activity-based probe (ABP)
Micheal addition
More stable intermediate mimic
B
BmDPA
Ub–BmDPA
pH 7.8, 37°C
15 min
IKZF3–Ub ABP
C
Ub–BmDPA
M (Calc.): 8666.6 Da
M (Obs.): 8665.0 Da
Normalized intensity (%)
m/z
Mass (kDa)
D
Rxn mix.
IKZF3–Ub ABP
Starting materials
kDa
IKZF3–Ub ABP
Ub–BmDPA/ /IKZF3
SEC fractions pooled
E
① NeCRL4CRBN
② IKZF3–Ub ABP
③ UbcH5a
④ Reaction mixture
⑤ Fraction pooled for cryo-EM
Thali
Lena
Poma
Mezig
Iber
Golca
Cemsi
Ava
DDB1
NeCUL4A
CRBN
Trapped product
UbcH5a
RBX1
ABP
CBB
F
SD200I SEC
SP6I SEC
Normalized A280
Elution volume (mL)

**Fig. S2. Implementing activity-based probe to trap the IMiD-induced IKZF3 ubiquitylation assemblies containing fully-activated $_{N8}$CRL4$^{CRBN}$ E3 ligase.**

(**A**) Diagram comparing the formation and geometry of the native transthiolation intermediate for IMiD-induced IKZF3 ubiquitylation and its more stable mimic. The mimic was generated through the Michael addition reaction between the activity-based probe (ABP) and the UbcH5a catalytic cysteine.

(**B**) Synthetic scheme of the IKZF3–Ub ABP. The IKZF3 ZF2–ZF3 K166C was conjugated to the C-terminal G75 of the donor Ub through a BmDPA handle.

(**C**) Electrospray ionization-mass spectrometry (ESI-MS) spectra and deconvoluted MS spectra of Ub–BmDPA with the calculated (Calc.) and observed (Obs.) molecular weight shown.

(**D**) SDS–PAGE analysis of the size-exclusion chromatography (SEC)-purified nucleophilic substitution reaction between Ub–BmDPA and IKZF3 ZF2–ZF3 K166C construct. Pooled fractions containing IKZF3–Ub ABP for structural study are indicated by the red rectangle.

(**E**) SDS–PAGE analysis of chemically-trapped ubiquitylation assembly formation in the presence of eight individual IMiD molecules. Fractions pooled for cryo-EM analysis were indicated by colored rectangles.

(**F**) Size-exclusion chromatograms of ubiquitylation assemblies containing eight individual IMiD molecules. The complex containing pomalidomide or mezigdomide was purified by a Superdex 200 Increase (SD200I) column (Cytiva, GE Healthcare). The complex containing thalidomide, lenalidomide, iberdomide, golcadomide, cemsidomide, or avadomide was purified by a Superose 6 Increase (SP6I) column (Cytiva, GE Healthcare).

# Figure S3

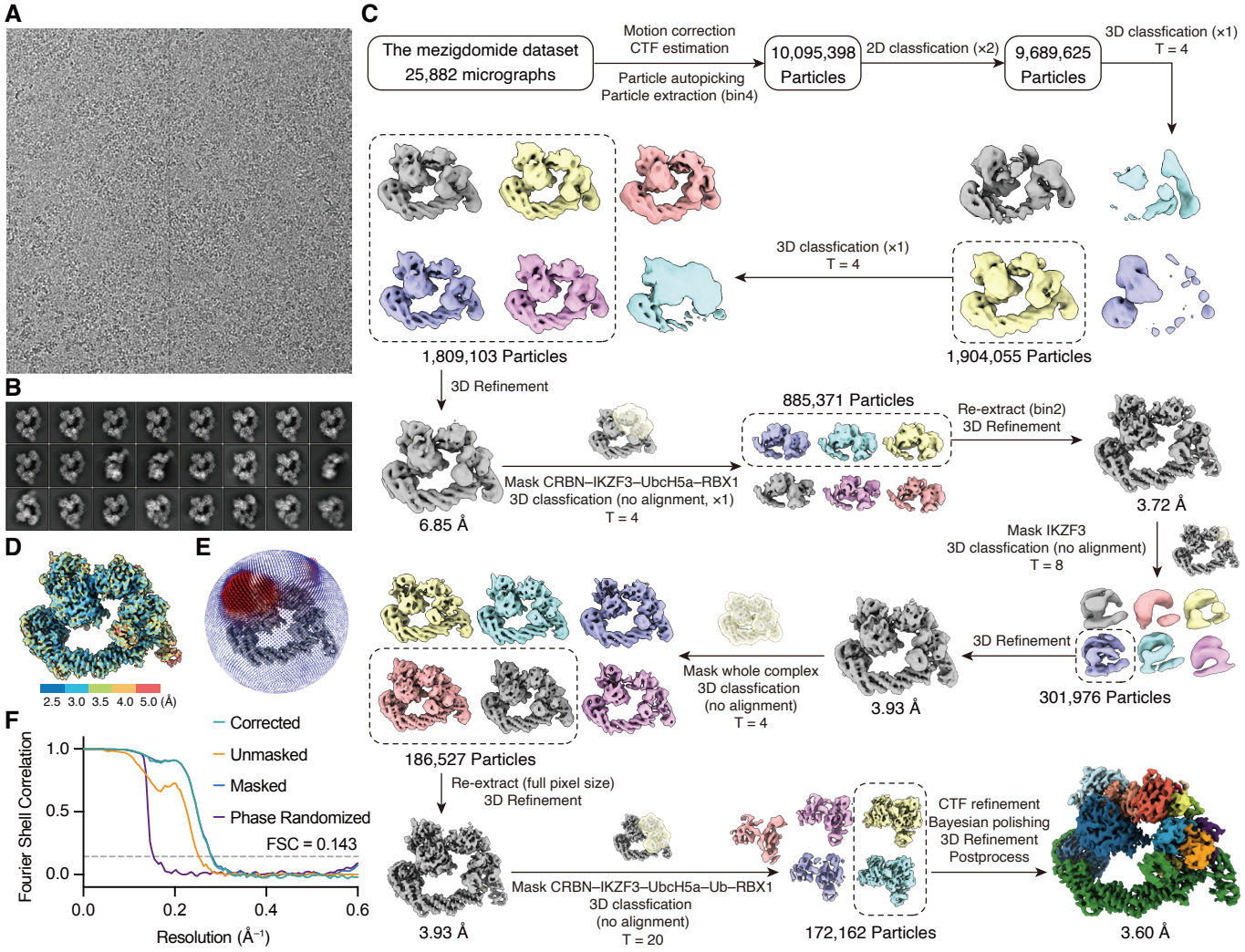
A
B
C
The mezigdomide dataset
25,882 micrographs
Motion correction
CTF estimation
Particle autopicking
Particle extraction (bin4)
10,095,398 Particles
2D classfication (×2)
9,689,625 Particles
3D classfication (×1)
T = 4
1,809,103 Particles
3D classfication (×1)
T = 4
1,904,055 Particles
3D Refinement
6.85 Å
Mask CRBN–IKZF3–UbcH5a–RBX1
3D classfication (no alignment, ×1)
T = 4
885,371 Particles
Re-extract (bin2)
3D Refinement
3.72 Å
Mask IKZF3
3D classfication (no alignment)
T = 8
301,976 Particles
3D Refinement
3.93 Å
Mask whole complex
3D classfication
(no alignment)
T = 4
186,527 Particles
Re-extract (full pixel size)
3D Refinement
3.93 Å
Mask CRBN–IKZF3–UbcH5a–Ub–RBX1
3D classfication
(no alignment)
T = 20
172,162 Particles
CTF refinement
Bayesian polishing
3D Refinement
Postprocess
3.60 Å
D
2.5 3.0 3.5 4.0 5.0 (Å)
E
F
Fourier Shell Correlation
1.0
0.5
0.0
0.0 0.2 0.4 0.6
Resolution (Å⁻¹)
Corrected
Unmasked
Masked
Phase Randomized
FSC = 0.143

**Fig. S3. Cryo-EM data processing flow chart of the mezigdomide-organized ubiquitylation assembly.**

(**A**) A representative micrograph.

(**B**) Representative 2D averages.

(**C**) Data processing workflow.

(**D**) Final cryo-EM map colored by the indicated local resolution.

(**E**) Angular distributions of the final cryo-EM reconstruction.

(**F**) Gold standard Fourier shell correlation (FSC) curves for the final refinement (3.60 Å resolution at FSC = 0.143).

# Figure S4

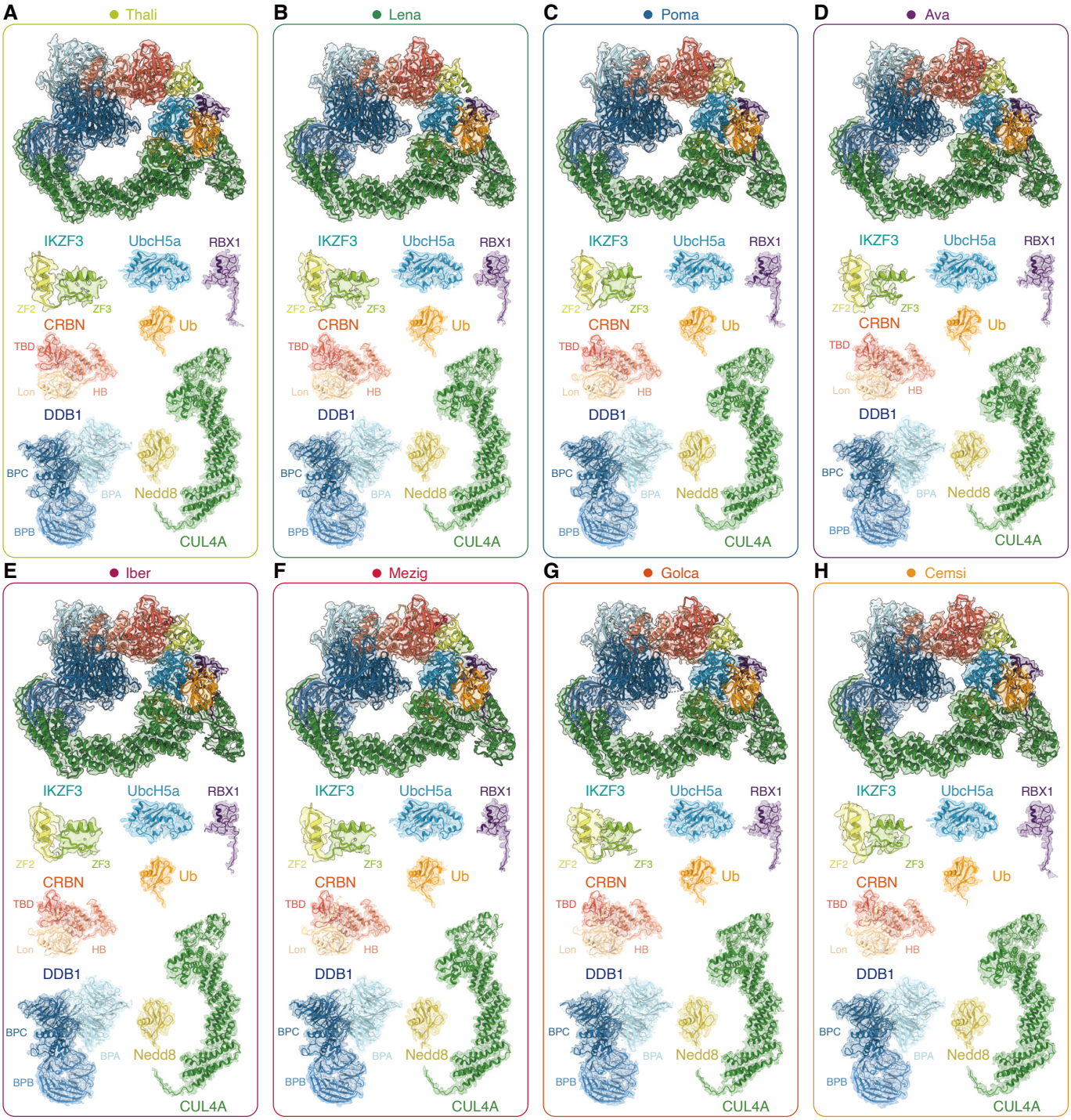
A
Thali
B
Lena
C
Poma
D
Ava
E
Iber
F
Mezig
G
Golca
H
Cemsi
IKZF3
UbcH5a
RBX1
ZF2
ZF3
CRBN
Ub
TBD
Lon
HB
DDB1
BPC
BPA
Nedd8
BPB
CUL4A

**Fig. S4. Cryo-EM density maps and atomic models of various components within the eight IMiD-organized ubiquitylation assemblies.**

(**A**) The thalidomide complex.

(**B**) The lenalidomide complex.

(**C**) The pomalidomide complex.

(**D**) The avadomide complex.

(**E**) The iberdomide complex.

(**F**) The mezigdomide complex.

(**G**) The golcadomide complex.

(**H**) The cemsidomide complex.

# Figure S5

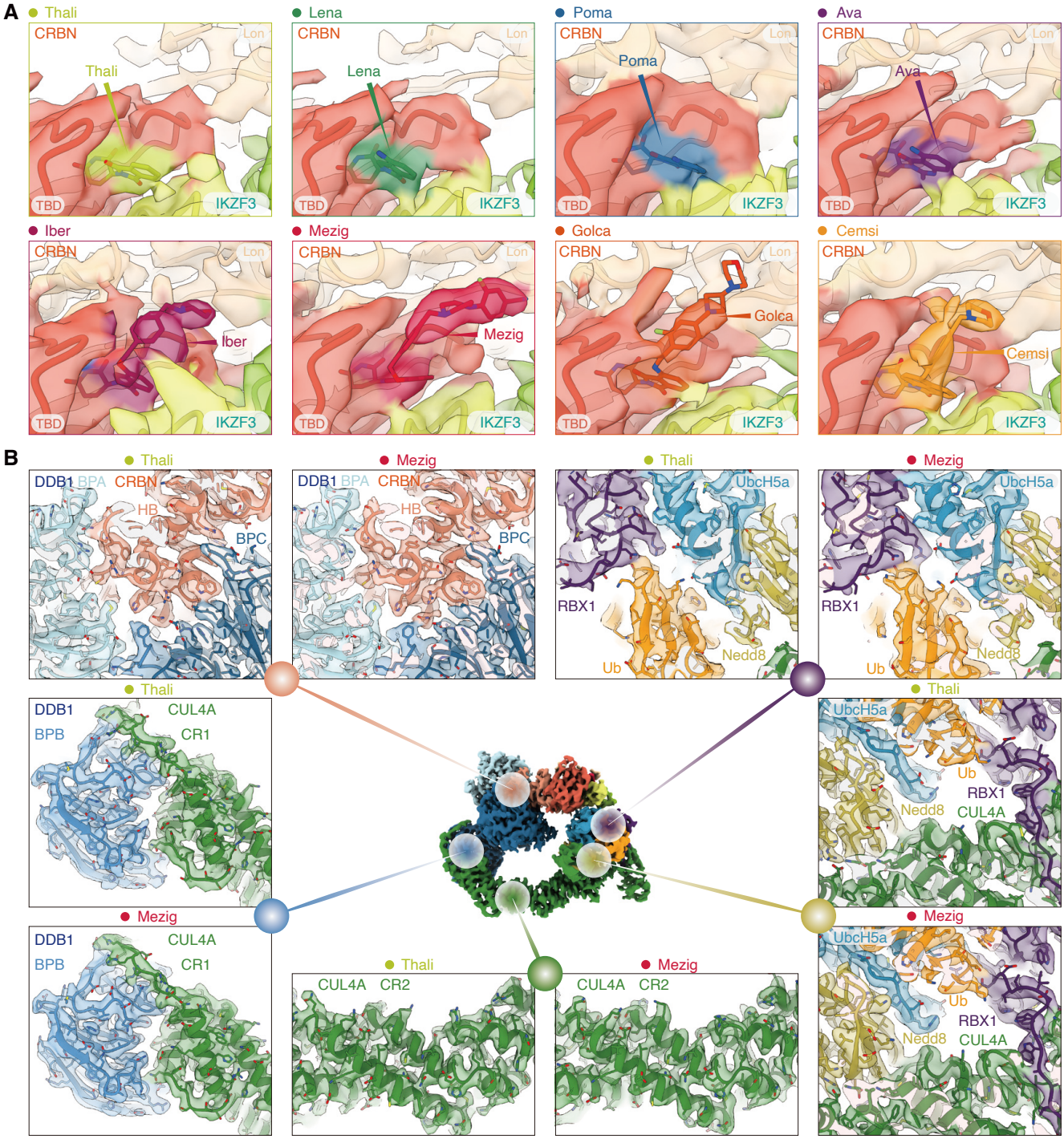
A
Thali
CRBN
Lon
Thali
TBD
IKZF3
Lena
CRBN
Lon
Lena
TBD
IKZF3
Poma
CRBN
Lon
Poma
TBD
IKZF3
Ava
CRBN
Lon
Ava
TBD
IKZF3
Iber
CRBN
Lon
Iber
TBD
IKZF3
Mezig
CRBN
Lon
Mezig
TBD
IKZF3
Golca
CRBN
Lon
Golca
TBD
IKZF3
Cemsi
CRBN
Cemsi
IKZF3
B
Thali
DDB1
BPA
CRBN
HB
BPC
Mezig
DDB1
BPA
CRBN
HB
BPC
Thali
UbcH5a
RBX1
Ub
Nedd8
Mezig
UbcH5a
RBX1
Ub
Nedd8
Thali
DDB1
CUL4A
BPB
CR1
Thali
UbcH5a
Ub
RBX1
Nedd8
CUL4A
Mezig
DDB1
CUL4A
BPB
CR1
Thali
CUL4A
CR2
Mezig
CUL4A
CR2
Mezig
UbcH5a
Ub
RBX1
Nedd8
CUL4A

**Fig. S5. Cryo-EM density maps and atomic models of key interacting regions of the eight IMiDs-organized ubiquitylation assemblies.**

(**A**) Substrate binding region in which eight individual IMiD molecules bind to the CRBN TBD pocket and IKZF3 ZF2 degron.

(**B**) Representative interfaces within the ubiquitylation assembly. The structures of complexes containing thalidomide or mezigdomide are exhibited as examples.

# Figure S6

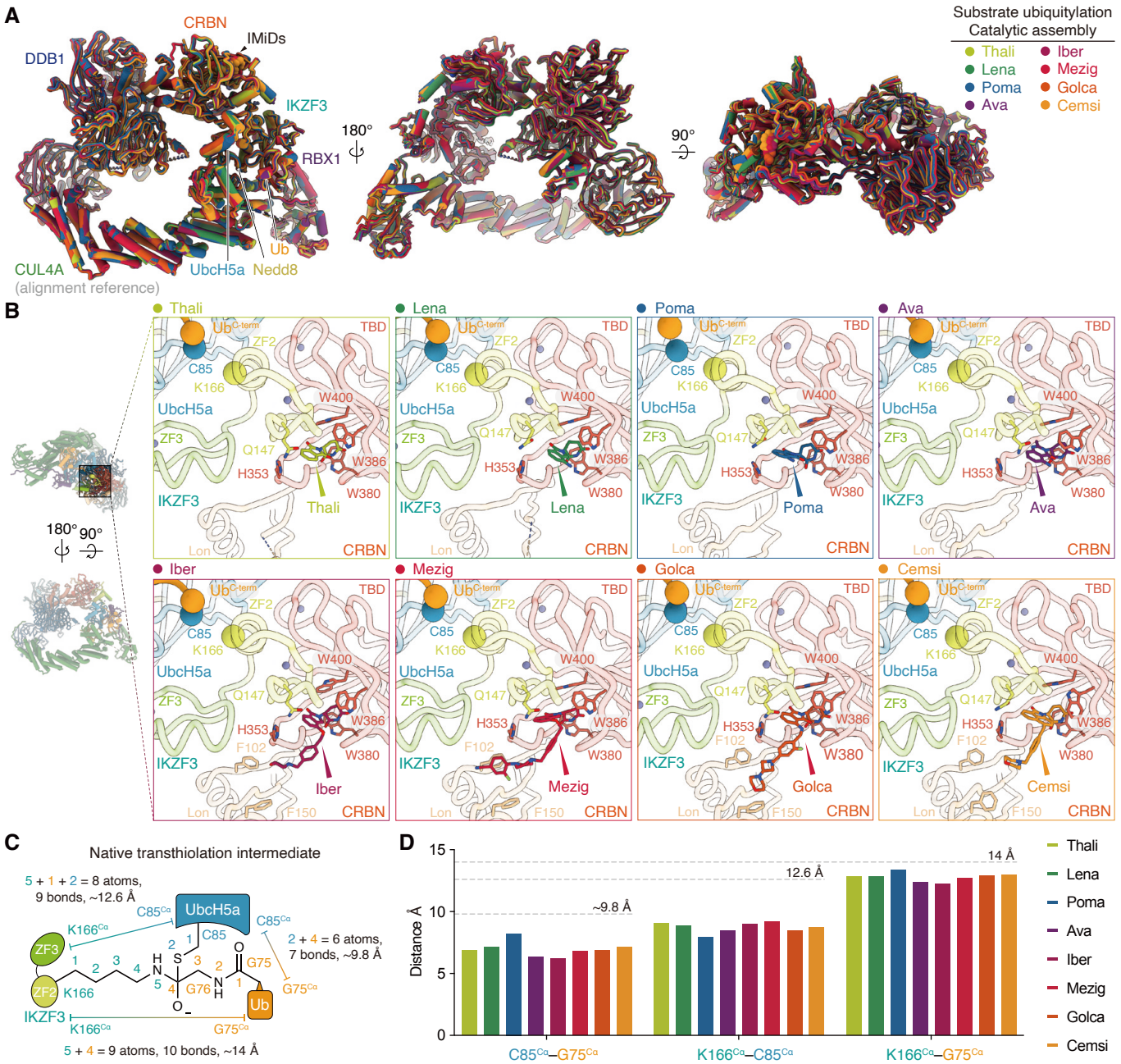
A
CRBN
IMiDs
DDB1
IKZF3
RBX1
Ub
CUL4A
UbcH5a
Nedd8
(alignment reference)
180°
90°
Substrate ubiquitylation
Catalytic assembly
Thali
Lena
Poma
Ava
Iber
Mezig
Golca
Cemsi
B
Thali
Lena
Poma
Ava
Iber
Mezig
Golca
Cemsi
Ub C-term
TBD
ZF2
C85
K166
UbcH5a
W400
ZF3
Q147
W386
H353
W380
IKZF3
F102
Lon
F150
CRBN
C
Native transthiolation intermediate
5 + 1 + 2 = 8 atoms,
9 bonds, ~12.6 Å
2 + 4 = 6 atoms,
7 bonds, ~9.8 Å
5 + 4 = 9 atoms, 10 bonds, ~14 Å
UbcH5a
ZF3
ZF2
IKZF3
Ub
G75
G76
D
Distance Å
~9.8 Å
12.6 Å
14 Å
C85Cα–G75Cα
K166Cα–C85Cα
K166Cα–G75Cα
Thali
Lena
Poma
Ava
Iber
Mezig
Golca
Cemsi

**Fig. S6. The tight organization of the active ubiquitylation assembly.**

(**A**) Three orientations of superposition of eight IMiD-organized ubiquitylation assembly structures. Structures were aligned based on CUL4A. A guide to coloring the eight structures is shown on the right.

(**B**) Zoomed-in views of the IMiD binding region and substrate ubiquitylation region in eight IMiD-organized ubiquitylation assemblies. Side chains of key interacting residues on CRBN and IKZF3 are shown as sticks. The Cα atoms of ubiquitylation site IKZF3 K166, UbcH5a catalytic cysteine C85, and Ub G75 are shown as spheres.

(**C**) Chemical structure and geometry of the native transthiolation intermediate in IMiD-organized ubiquitylation assembly. The spatial distance between each crosslinking site was estimated based on the number of covalent bonds involved, multiplied by the theoretical bond length of a carbon–carbon single bond (~1.4 Å per bond). This approximation provides an upper-bound estimate of the spatial distance under the assumption of fully extended bond geometries.

(**D**) Bar graph showing the spatial distance between each crosslinking site measured across the eight IMiD-organized ubiquitylation assemblies. The upper-bound estimates of the spatial distance are indicated by gray dashed lines.

# Figure S7

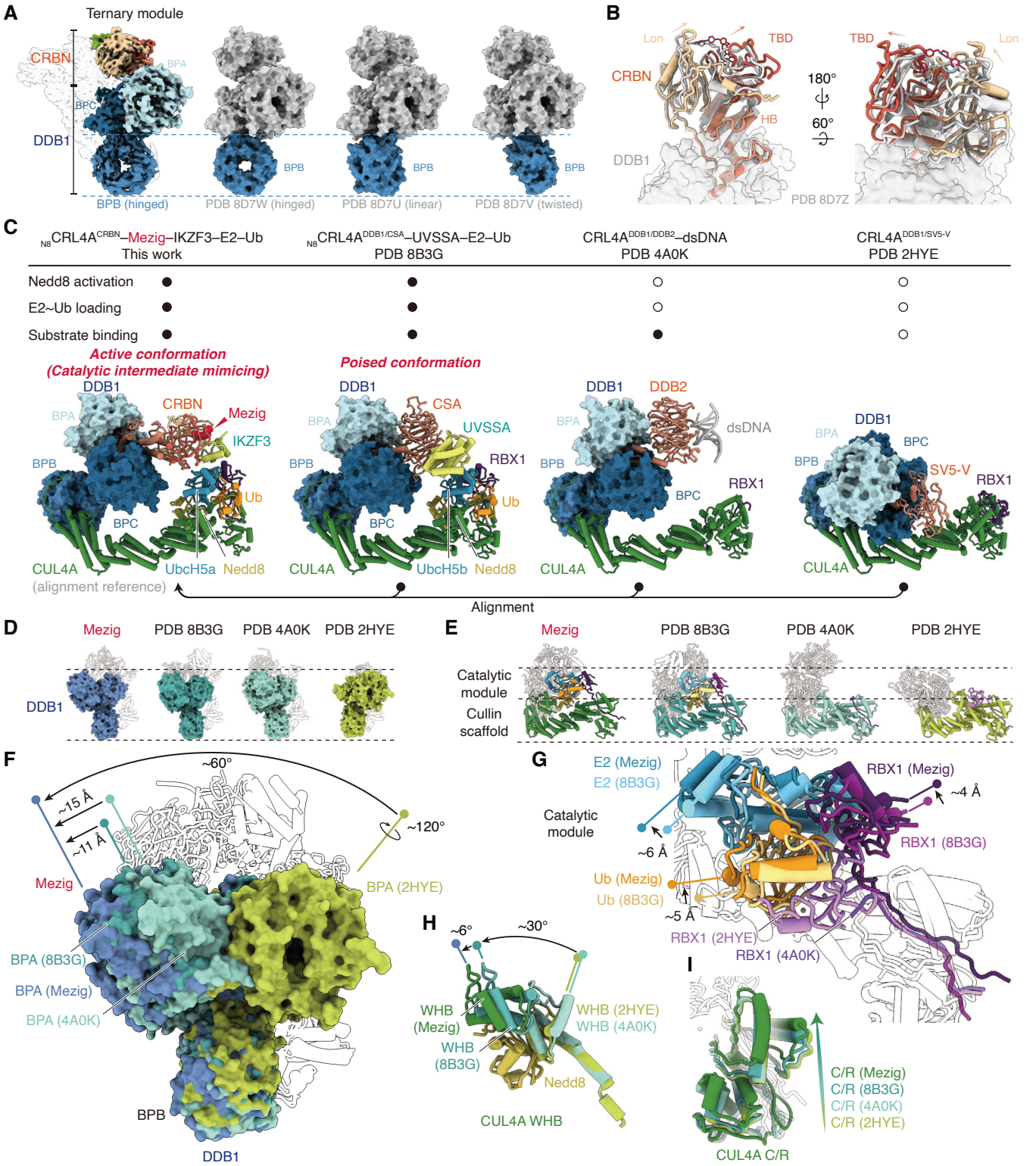
A
Ternary module
CRBN
BPA
BPC
DDB1
BPB
BPB (hinged)
PDB 8D7W (hinged)
PDB 8D7U (linear)
PDB 8D7V (twisted)
B
Lon
TBD
CRBN
HB
DDB1
180°
60°
PDB 8D7Z
C
N8CRL4ACRBN–Mezig–IKZF3–E2–Ub
This work
N8CRL4ADDB1/CSA–UVSSA–E2–Ub
PDB 8B3G
CRL4ADDB1/DDB2–dsDNA
PDB 4A0K
CRL4ADDB1/SV5-V
PDB 2HYE
Nedd8 activation
E2~Ub loading
Substrate binding
Active conformation
(Catalytic intermediate mimicing)
Poised conformation
Mezig
IKZF3
Ub
UbcH5a
Nedd8
CSA
UVSSA
RBX1
UbcH5b
DDB2
dsDNA
SV5-V
CUL4A
(alignment reference)
Alignment
D
Mezig
PDB 8B3G
PDB 4A0K
PDB 2HYE
E
Catalytic module
Cullin scaffold
F
~60°
~15 Å
~11 Å
~120°
BPA (2HYE)
BPA (8B3G)
BPA (Mezig)
BPA (4A0K)
G
E2 (Mezig)
E2 (8B3G)
RBX1 (Mezig)
~4 Å
RBX1 (8B3G)
~6 Å
Ub (Mezig)
Ub (8B3G)
~5 Å
RBX1 (2HYE)
RBX1 (4A0K)
H
~6°
~30°
WHB (Mezig)
WHB (8B3G)
WHB (2HYE)
WHB (4A0K)
CUL4A WHB
I
C/R (Mezig)
C/R (8B3G)
C/R (4A0K)
C/R (2HYE)
CUL4A C/R

**Fig. S7. Striking conformational flexibility of the $_{N8}CRL4^{CRBN}$ E3 ligase in catalyzing IMiD-induced neosubstrate ubiquitylation and different inactive states.**

(**A**) Cryo-EM map of CRBN/DDB1 in the ternary module within the mezigdomide-organized ubiquitylation assembly and surface presentations of reported mezigdomide-liganded CRBN/DDB1 in three discrete conformations (hinged, PDB 8D7W; linear, PDB 8D7U; twisted, PDB 8D7V) are shown from the same orientation. The CUL4A-interacting DDB1 BPB domain (colored blue) in the ubiquitylation assembly adopts the hinged conformation.

(**B**) Structural alignment of CRBN/DDB1 within the mezigdomide-organized ubiquitylation assembly and reported mezigdomide-liganded CRBN/DDB1 ternary complex (PDB 8D7Z). The substrates in these structures were hidden for clarity. Conformational changes are indicated by arrows.

(**C**) Description and cartoon models of four reported structures representing different states of the CRL4A E3 ligase complex. States were defined according to Nedd8 activation status, E2~Ub loading, and substrate binding. Structures were aligned to the Mezig structure based on CUL4A for further analysis in **D**–**I**.

(**D**) Surface presentations of DDB1 in the four structures are shown from the same orientation. Other components are contoured by black lines.

(**E**) Cartoon presentations of the catalytic module and/or cullin scaffold in the four structures are shown from the same orientation. Other components are contoured by black lines.

(**F**) Superposition of the four structures, highlighting the stepwise conformational changes of the DDB1 BPA domain.

(**G**) Superposition of the four structures, highlighting the stepwise conformational changes of the catalytic module containing RBX1 and E2~Ub.

(**H**) Superposition of the four structures, highlighting the stepwise conformational changes of the CUL4A WHB domain.

(**I**) Superposition of the four structures, highlighting the stepwise conformational changes of the CUL4A C/R domain.

# Figure S8

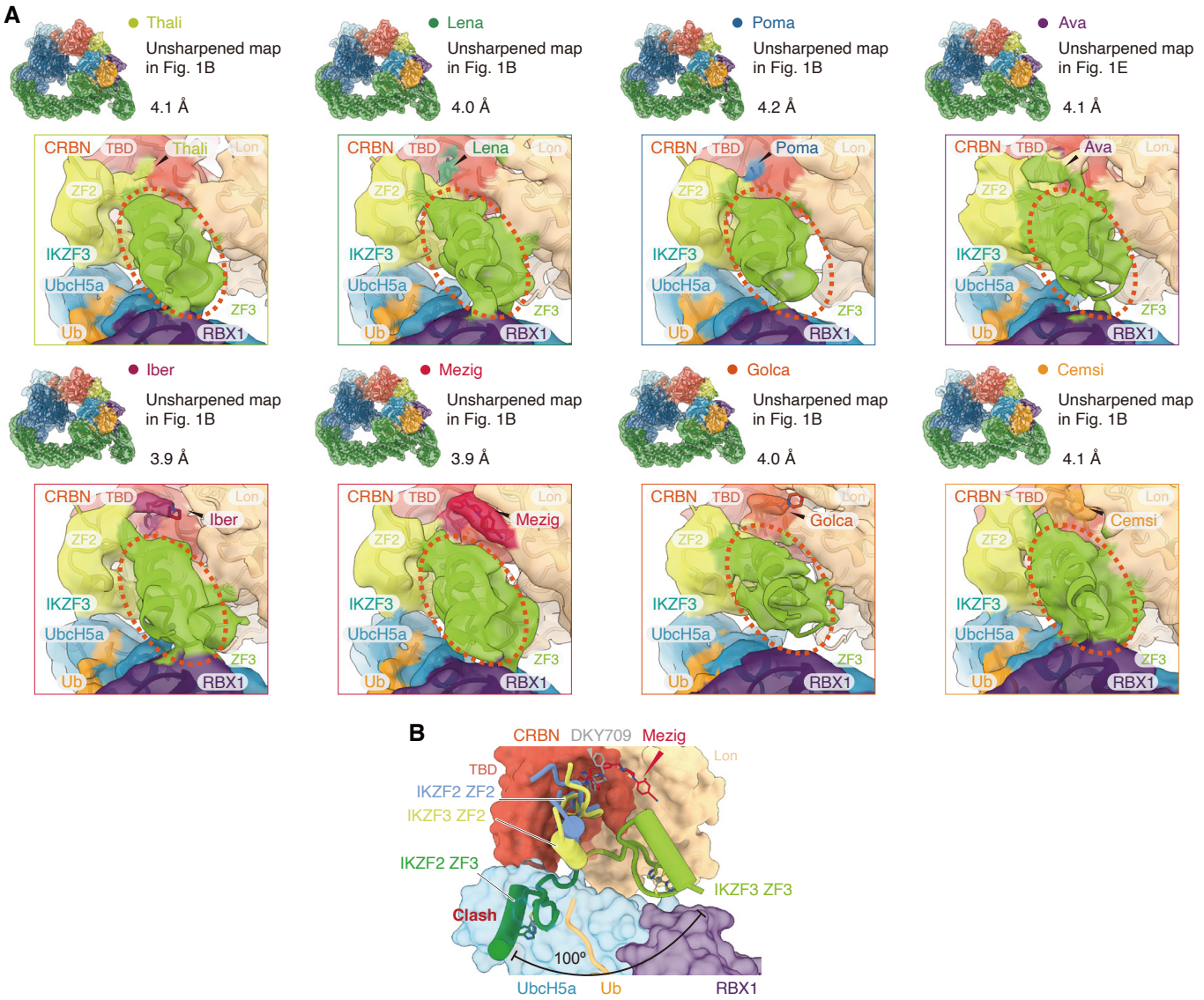
A
Thali
Unsharpened map in Fig. 1B
4.1 Å
Lena
Unsharpened map in Fig. 1B
4.0 Å
Poma
Unsharpened map in Fig. 1B
4.2 Å
Ava
Unsharpened map in Fig. 1E
4.1 Å
Iber
Unsharpened map in Fig. 1B
3.9 Å
Mezig
Unsharpened map in Fig. 1B
3.9 Å
Golca
Unsharpened map in Fig. 1B
4.0 Å
Cemsi
Unsharpened map in Fig. 1B
4.1 Å
CRBN
TBD
Lon
ZF2
IKZF3
UbcH5a
ZF3
Ub
RBX1
B
CRBN
DKY709
Mezig
Lon
TBD
IKZF2 ZF2
IKZF3 ZF2
IKZF2 ZF3
IKZF3 ZF3
Clash
100°
UbcH5a
Ub
RBX1

**Fig. S8. Unexpected cryo-EM density of IKZF3 ZF3 bridges the CRBN Lon domain and RBX1/UbcH5a.**

(**A**) Zoomed-in views of unsharpened cryo-EM maps of eight IMiD-organized ubiquitylation assemblies. Red dashed circles highlight densities of the IKZF3 ZF3 motif.

(**B**) Superposition of the mezigdomide-organized ubiquitylation assembly structure and the IKZF2–DKY709–CRBN/DDB1 ternary complex (PDB 8DEY) structure. Spatial differences in the positioning of the ZF3 motifs and potential steric clashes are indicated.

# Figure S9

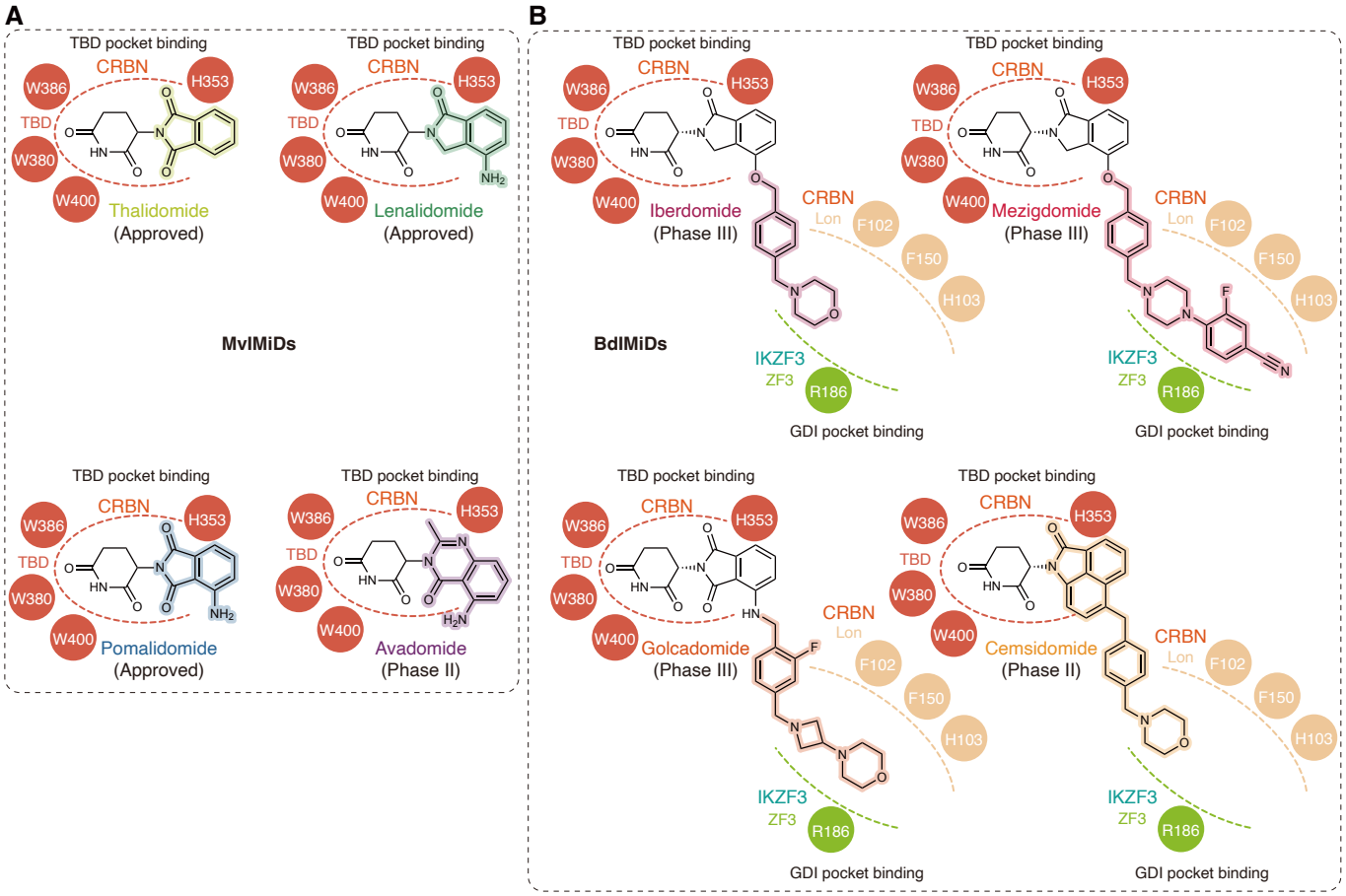
A
TBD pocket binding
CRBN
W386
H353
TBD
W380
W400
Thalidomide
(Approved)
Lenalidomide
(Approved)
MvIMiDs
Pomalidomide
(Approved)
Avadomide
(Phase II)
B
BdIMiDs
Iberdomide
(Phase III)
Mezigdomide
(Phase III)
Golcadomide
(Phase III)
Cemsidomide
(Phase II)
Lon
F102
F150
H103
IKZF3
ZF3
R186
GDI pocket binding

**Fig. S9. Comparison of IMiDs' chemical structures and interactions with CRBN/IKZF3.**

(**A**, **B**) Schematic IMiD–TBD pocket interactions and IMiD–GDI pocket interactions of MvIMiDs (**A**) or BdIMiDs (**B**).

# Figure S10

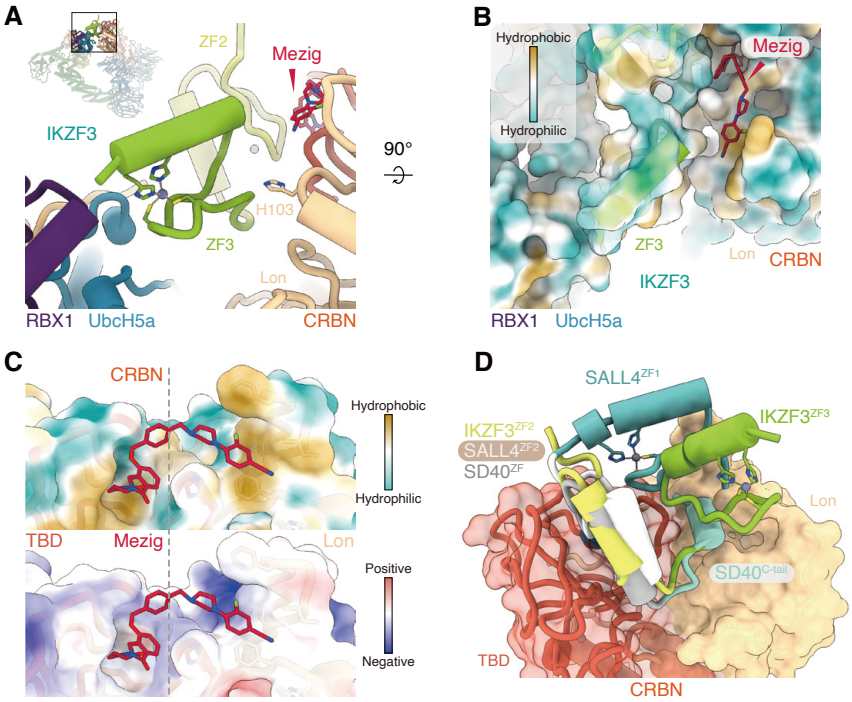
A
ZF2
Mezig
IKZF3
90°
H103
ZF3
Lon
RBX1
UbcH5a
CRBN
B
Hydrophobic
Hydrophilic
Mezig
ZF3
Lon
CRBN
IKZF3
RBX1
UbcH5a
C
CRBN
Hydrophobic
Hydrophilic
TBD
Mezig
Lon
Positive
Negative
D
SALL4ZF1
IKZF3ZF2
SALL4ZF2
SD40ZF
IKZF3ZF3
Lon
SD40C-tail
TBD
CRBN

**Fig. S10. CRBN Lon domain provides an interface for the synergistic binding of IMiDs and zinc finger proteins.**

(**A**) Detailed view shows IKZF3 ZF3 bridging the CRBN Lon domain and RBX1/UbcH5a.

(**B**) The hydrophobic/hydrophilic surface properties of IKZF3, CRBN, RBX1, and UbcH5a.

(**C**) The hydrophobic/hydrophilic properties (top) and electrostatic properties (bottom) of the CRBN TBD and Lon surface binding with mezigdomide.

(**D**) Structural alignments of the IKZF3–mezigdomide–CRBN/DDB1 ternary module (this work), the SALL4–iberdomide–CRBN/DDB1 ternary complex (PDB 8U16), and SD40–PT-179–CRBN/DDB1 ternary complex (PDB 8TNP), showing various zinc finger proteins binding to the CRBN Lon surface.

# Figure S11

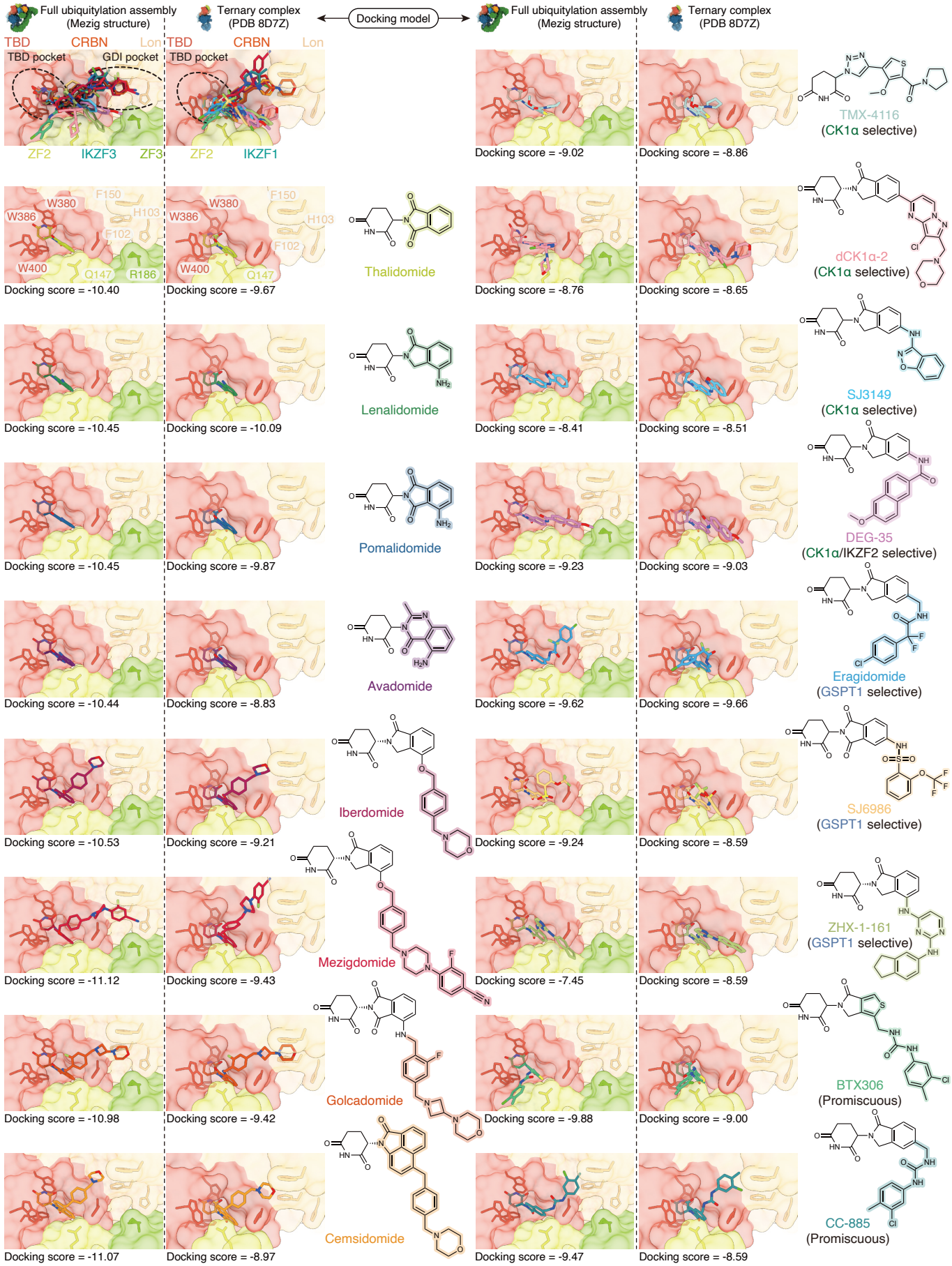
Full ubiquitylation assembly (Mezig structure)
Ternary complex (PDB 8D7Z)
Docking model
Full ubiquitylation assembly (Mezig structure)
Ternary complex (PDB 8D7Z)
TBD
CRBN
Lon
TBD pocket
GDI pocket
ZF2
IKZF3
ZF3
IKZF1
W380
W386
F150
H103
F102
W400
Q147
R186
Docking score = -9.02
Docking score = -8.86
TMX-4116
(CK1α selective)
Docking score = -10.40
Docking score = -9.67
Thalidomide
Docking score = -8.76
Docking score = -8.65
dCK1α-2
(CK1α selective)
Docking score = -10.45
Docking score = -10.09
Lenalidomide
Docking score = -8.41
Docking score = -8.51
SJ3149
(CK1α selective)
Docking score = -10.45
Docking score = -9.87
Pomalidomide
Docking score = -9.23
Docking score = -9.03
DEG-35
(CK1α/IKZF2 selective)
Docking score = -10.44
Docking score = -8.83
Avadomide
Docking score = -9.62
Docking score = -9.66
Eragidomide
(GSPT1 selective)
Docking score = -10.53
Docking score = -9.21
Iberdomide
Docking score = -9.24
Docking score = -8.59
SJ6986
(GSPT1 selective)
Docking score = -11.12
Docking score = -9.43
Mezigdomide
Docking score = -7.45
Docking score = -8.59
ZHX-1-161
(GSPT1 selective)
Docking score = -10.98
Docking score = -9.42
Golcadomide
Docking score = -9.88
Docking score = -9.00
BTX306
(Promiscuous)
Docking score = -11.07
Docking score = -8.97
Cemsidomide
Docking score = -9.47
Docking score = -8.59
CC-885
(Promiscuous)

**Fig. S11. Docking poses of IMiDs with distinct substrate selectivities within the full ubiquitylation complex or ternary complex.**

Docking poses and docking scores of each IMiD molecule in the CRBN TBD pocket and/or GDI pocket. CRBN and IKZF1/3 are shown as surface representations. Side chains of key CRBN and IKZF1/3 interacting residues, including CRBN H103, F102, F150, H353, W380, W386, W400, IKZF3 Q147 (IKZF1 Q146), and IKZF3 R186 are indicated. Chemical structures of each IMiD molecule are shown beside the docking model.

# Figure S12

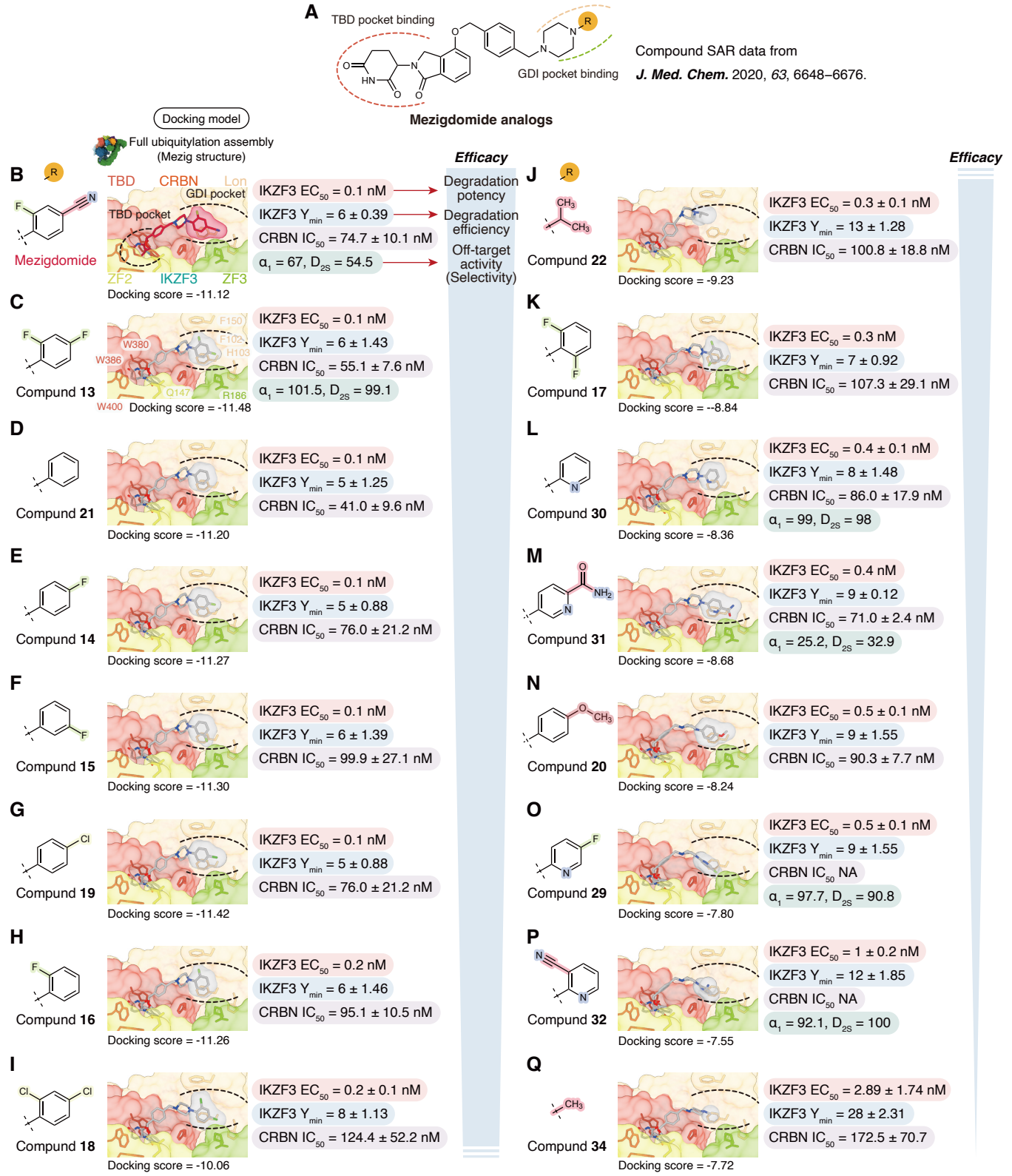
A
TBD pocket binding
GDI pocket binding
Mezigdomide analogs
Compound SAR data from
J. Med. Chem. 2020, 63, 6648–6676.
Docking model
Full ubiquitylation assembly
(Mezig structure)
Efficacy
TBD
CRBN
Lon
GDI pocket
TBD pocket
ZF2
IKZF3
ZF3
Mezigdomide
Docking score = -11.12
IKZF3 EC50 = 0.1 nM
IKZF3 Ymin = 6 ± 0.39
CRBN IC50 = 74.7 ± 10.1 nM
α1 = 67, D2S = 54.5
Degradation potency
Degradation efficiency
Off-target activity (Selectivity)
B
C
Compund 13
Docking score = -11.48
IKZF3 EC50 = 0.1 nM
IKZF3 Ymin = 6 ± 1.43
CRBN IC50 = 55.1 ± 7.6 nM
α1 = 101.5, D2S = 99.1
D
Compund 21
Docking score = -11.20
IKZF3 EC50 = 0.1 nM
IKZF3 Ymin = 5 ± 1.25
CRBN IC50 = 41.0 ± 9.6 nM
E
Compund 14
Docking score = -11.27
IKZF3 EC50 = 0.1 nM
IKZF3 Ymin = 5 ± 0.88
CRBN IC50 = 76.0 ± 21.2 nM
F
Compund 15
Docking score = -11.30
IKZF3 EC50 = 0.1 nM
IKZF3 Ymin = 6 ± 1.39
CRBN IC50 = 99.9 ± 27.1 nM
G
Compund 19
Docking score = -11.42
IKZF3 EC50 = 0.1 nM
IKZF3 Ymin = 5 ± 0.88
CRBN IC50 = 76.0 ± 21.2 nM
H
Compund 16
Docking score = -11.26
IKZF3 EC50 = 0.2 nM
IKZF3 Ymin = 6 ± 1.46
CRBN IC50 = 95.1 ± 10.5 nM
I
Compund 18
Docking score = -10.06
IKZF3 EC50 = 0.2 ± 0.1 nM
IKZF3 Ymin = 8 ± 1.13
CRBN IC50 = 124.4 ± 52.2 nM
J
Compund 22
Docking score = -9.23
IKZF3 EC50 = 0.3 ± 0.1 nM
IKZF3 Ymin = 13 ± 1.28
CRBN IC50 = 100.8 ± 18.8 nM
K
Compund 17
Docking score = --8.84
IKZF3 EC50 = 0.3 nM
IKZF3 Ymin = 7 ± 0.92
CRBN IC50 = 107.3 ± 29.1 nM
L
Compund 30
Docking score = -8.36
IKZF3 EC50 = 0.4 ± 0.1 nM
IKZF3 Ymin = 8 ± 1.48
CRBN IC50 = 86.0 ± 17.9 nM
α1 = 99, D2S = 98
M
Compund 31
Docking score = -8.68
IKZF3 EC50 = 0.4 nM
IKZF3 Ymin = 9 ± 0.12
CRBN IC50 = 71.0 ± 2.4 nM
α1 = 25.2, D2S = 32.9
N
Compund 20
Docking score = -8.24
IKZF3 EC50 = 0.5 ± 0.1 nM
IKZF3 Ymin = 9 ± 1.55
CRBN IC50 = 90.3 ± 7.7 nM
O
Compund 29
Docking score = -7.80
IKZF3 EC50 = 0.5 ± 0.1 nM
IKZF3 Ymin = 9 ± 1.55
CRBN IC50 NA
α1 = 97.7, D2S = 90.8
P
Compund 32
Docking score = -7.55
IKZF3 EC50 = 1 ± 0.2 nM
IKZF3 Ymin = 12 ± 1.85
CRBN IC50 NA
α1 = 92.1, D2S = 100
Q
Compund 34
Docking score = -7.72
IKZF3 EC50 = 2.89 ± 1.74 nM
IKZF3 Ymin = 28 ± 2.31
CRBN IC50 = 172.5 ± 70.7

**Fig. S12. Understanding the structure-activity relationship (SAR) of mezigdomide analogs through GDI pocket interacting models.**

(**A**) Chemical structure of mezigdomide analogs. The terminal functional group conjugated to the piperizine moiety is indicated by the "R" group.

(**B**–**Q**) The chemical structure of the R group in each mezigdomide analog (left), the docking model and docking scores of the analog within the full ubiquitylation complex (middle), and reported SAR data (right). For SAR data, IKZF3 EC50 indicates the degradation potency. IKZF3 $Y_{min}$, the protein remaining after drug treatment, indicates the degradation efficiency. Value of $\alpha_1$ and $D_{2S}$ mean percent inhibition of $\alpha_1$ adrenergic receptor and dopamine $D_{2S}$ receptor, which indicates off-target activity (or selectivity). The reported compounds are ranked from high to low efficacy, as indicated by the light blue arrow. The most striking difference arises from the comparison between compound **34** (**Q**) and other analogs: replacing the terminal aromatic ring with a smaller methyl group significantly reduces compatibility with the GDI pocket, accompanied by a marked impairment in IKZF3 EC50, $Y_{min}$, and CRBN IC50 values. The substitution of the 4-nitrile group (**B**) with a fluorine atom (**C**) compromises the fit within the GDI pocket, which is associated with a notable decline in the selectivity of the drug.

**Table S1. Cryo-EM data collection, refinement, and validation statistics for MvIMiD structures.**

| | $_{N8}$CRL4$^{CRBN}$–IMiD–IKZF3(ZF2–ZF3)–UbcH5a–Ub complex | | | |
|---|---|---|---|---|
| **MvIMiDs** | Thalidomide | Lenalidomide | Pomalidomide | Avadomide |
| **PDB entry** | 9UUQ | 9V09 | 9V0A | 9V0B |
| **EMDB entry** | EMD-64515 | EMD-64658 | EMD-64659 | EMD-64660 |
| **Data collection & processing** | | | | |
| **Microscope and detector** | Krios G4/Falcon4 | Krios G4/Falcon4 | Krios/K3 | Krios G4/Falcon4 |
| **Magnification** | 75,000 | 75,000 | 81,000 | 75,000 |
| **Voltage (keV)** | 300 | 300 | 300 | 300 |
| **Electron exposure ($e^-$/Å$^2$)** | 50 | 50 | 50 | 50 |
| **Defocus range (µm)** | –1.2 to –2.0 | –1.2 to –2.0 | –1.0 to –1.8 | –1.2 to –2.0 |
| **Pixel size (Å)** | 1.059 | 1.059 | 1.074 | 1.059 |
| **Symmetry imposed** | C1 | C1 | C1 | C1 |
| **Micrographs (no.)** | 7,706 | 7,621 | 13,668 | 8,474 |
| **Final particles (no.)** | 62,925 | 89,694 | 180,420 | 60,674 |
| **Map global resolution (Å)** | 3.61 | 3.51 | 3.82 | 3.61 |
| **FSC threshold** | 0.143 | 0.143 | 0.143 | 0.143 |
| **$CC_{mask}/CC_{volume}$** | 0.78/0.77 | 0.77/0.76 | 0.81/0.81 | 0.76/0.74 |
| **B-factor (Å$^2$)** | –70 | –70 | –100 | –80 |
| **Refinement & validation** | | | | |
| **Initial model** | PDB 8B3G, 8D7Z; AF-Q9UKT9-F1-v4 | PDB 8B3G, 8D7Z; AF-Q9UKT9-F1-v4 | PDB 8B3G, 8D7Z; AF-Q9UKT9-F1-v4 | PDB 8B3G, 8D7Z; AF-Q9UKT9-F1-v4 |
| **Model composition** | | | | |
| **Non-hydrogen atoms** | 20,534 | 20,551 | 20,824 | 20,732 |
| **Protein residues** | 2,581 | 2,586 | 2,616 | 2,614 |
| **Ligands** | 6 Zn, 1 Thali | 6 Zn, 1 Lena | 6 Zn, 1 Poma | 6 Zn, 1 Ava |
| **R.M.S. deviations** | | | | |
| **Bond lengths (Å)** | 0.003 | 0.003 | 0.004 | 0.003 |
| **Bond angles (°)** | 0.682 | 0.669 | 0.699 | 0.660 |
| **B-factor (Å$^2$)** | | | | |
| **Protein (min/max/mean)** | 30.00/246.66/102.14 | 21.23/323.37/89.54 | 30.00/324.79/137.67 | 17.58/240.23/84.91 |
| **Ligand (min/max/mean)** | 81.62/243.30/95.94 | 90.92/328.46/108.60 | 115.58/297.18/143.28 | 67.33/237.36/82.61 |
| **MolProbity score** | 1.78 | 1.80 | 1.92 | 1.78 |
| **Clashscore** | 7.10 | 7.54 | 10.53 | 7.02 |
| **Rotamer outliers (%)** | 0.13 | 0.04 | 0.04 | 0 |
| **CaBLAM outliers (%)** | 2.62 | 2.69 | 3.01 | 3.32 |
| **Ramachandran plot** | | | | |
| **Favored (%)** | 94.31 | 94.37 | 94.63 | 94.28 |
| **Allowed (%)** | 5.69 | 5.63 | 5.37 | 5.72 |
| **Outliers (%)** | 0 | 0 | 0 | 0 |

**Table S2. Cryo-EM data collection, refinement, and validation statistics for BdIMiD structures.**

| | $_{N8}$CRL4$^{CRBN}$–IMiD–IKZF3(ZF2–ZF3)–UbcH5a–Ub complex | | | |
|---|---|---|---|---|
| **BdIMiDs** | Iberdomide | Mezigdomide | Golcadomide | Cemsidomide |
| **PDB entry** | 9V0C | 9UUM | 9V0E | 9V0F |
| **EMDB entry** | EMD-64661 | EMD-64512 | EMD-64662 | EMD-64663 |
| **Data collection & processing** | | | | |
| **Microscope and detector** | Krios G4/Falcon4 | Krios G4/Falcon4 | Krios G4/Falcon4 | Krios G4/Falcon4 |
| **Magnification** | 75,000 | 96,000 | 75,000 | 75,000 |
| **Voltage (keV)** | 300 | 300 | 300 | 300 |
| **Electron exposure ($e^-$/Å$^2$)** | 50 | 50 | 50 | 50 |
| **Defocus range (µm)** | –1.2 to –2.0 | –1.2 to –2.0 | –1.2 to –2.0 | –1.2 to –2.0 |
| **Pixel size (Å)** | 1.059 | 0.83 | 1.059 | 1.059 |
| **Symmetry imposed** | C1 | C1 | C1 | C1 |
| **Micrographs (no.)** | 8,097 | 25,882 | 8,567 | 7,205 |
| **Final particles (no.)** | 42,369 | 172,162 | 37,205 | 48,755 |
| **Map global resolution (Å)** | 3.46 | 3.60 | 3.60 | 3.71 |
| **FSC threshold** | 0.143 | 0.143 | 0.143 | 0.143 |
| **$CC_{mask}/CC_{volume}$** | 0.79/0.78 | 0.81/0.78 | 0.70/0.69 | 0.77/0.76 |
| **B-factor (Å$^2$)** | –70 | –100 | –80 | –50 |
| **Refinement & validation** | | | | |
| **Initial model** | PDB 8B3G, 8D7Z; AF-Q9UKT9-F1-v4 | PDB 8B3G, 8D7Z; AF-Q9UKT9-F1-v4 | PDB 8B3G, 8D7Z; AF-Q9UKT9-F1-v4 | PDB 8B3G, 8D7Z; AF-Q9UKT9-F1-v4 |
| **Model composition** | | | | |
| **Non-hydrogen atoms** | 20,746 | 20,808 | 20,776 | 20,720 |
| **Protein residues** | 2,614 | 2,620 | 2,614 | 2,615 |
| **Ligands** | 6 Zn, 1 Iberdomide | 6 Zn, 1 Mezigdomide | 6 Zn, 1 Golcadomide | 6 Zn, 1 Cemsidomide |
| **R.M.S. deviations** | | | | |
| **Bond lengths (Å)** | 0.003 | 0.003 | 0.003 | 0.003 |
| **Bond angles (°)** | 0.669 | 0.626 | 0.569 | 0.695 |
| **B-factor (Å$^2$)** | | | | |
| **Protein (min/max/mean)** | 16.82/318.87/108.30 | 1.61/337.60/73.75 | 23.57/217.01/88.36 | 47.29/275.76/107.96 |
| **Ligand (min/max/mean)** | 84.78/234.61/116.96 | 63.10/171.33/70.48 | 34.39/133.74/89.09 | 108.61/311.36/120.29 |
| **MolProbity score** | 1.77 | 1.77 | 1.82 | 1.90 |
| **Clashscore** | 7.11 | 6.85 | 8.17 | 7.65 |
| **Rotamer outliers (%)** | 0 | 0.09 | 0 | 0 |
| **CaBLAM outliers (%)** | 2.58 | 2.77 | 3.01 | 3.24 |
| **Ramachandran plot** | | | | |
| **Favored (%)** | 94.43 | 94.25 | 94.51 | 92.35 |
| **Allowed (%)** | 5.57 | 5.75 | 5.45 | 7.65 |
| **Outliers (%)** | 0 | 0 | 0 | 0 |

**Table S3. Summary of reported binary or ternary complex structures in the PDB database that contain the eight IKZF1/3-targeting IMiDs examined in this study.**

| IMiDs | Number of binary complex | PDB Accession codes | Number of ternary complex | PDB Accession codes |
|---|---|---|---|---|
| **Thali** | 23 | 4CI1, 4TZC, 4V2Y, 4V32, 5AMH, 5AMI, 5AMJ, 5AMK, 5OH1, 5YIZ, 5YJ0, 6R0S, 6R0U, 6R12, 6R13, 6R18, 6R19, 6R1A, 6R1C, 6R1W 7PSO, 8BC7, 8OU3 | 1 | 7BQU |
| **Lena** | 5 | 4CI2, 4TZ4, 4V30, 9FJX, 8RQA | 1 | 5FQD |
| **Poma** | 5 | 4CI3, 4TZU, 4V2Z, 8D81, 8OIZ, | 7 | 6H0F, 6H0G, 6UML,8TNP, 8U15, 8U16, 8U17 |
| **Ava** | 1 | 7PSO | 0 | |
| **Iber** | 2 | 5V3O, 7PS9 | 2 | 8D80, 8U15 |
| **Mezig** | 4 | 8RQ8, 8D7U, 8D7V, 8D7W | 2 | 8RQC，8D7Z |
| **Golca** | 0 | -- | 0 | -- |
| **Cemsi** | 0 | -- | 0 | -- |

Data as of March 20, 2025.

**Caption for Data S1 to S3**

**Data S1. (separate PDF file)**

Cryo-EM data processing flow chart of seven IMiD-organized ubiquitylation assemblies (thalidomide, lenalidomide, pomalidomide, avadomide, iberdomide, golcadomide, and cemsidomide).

**Data S2. (separate PDF file)**

Uncropped gel images for blots and *in vitro* ubiquitylation assays for *in vivo* degradation assays.

**Data S3. (separate PDF file)**

Gel images for SDS–PAGE analysis of recombinant proteins and corresponding mutants used in this study.

**References**


1. Z. Deng *et al.*, Mechanistic insights into nucleosomal H2B monoubiquitylation mediated by yeast Bre1-Rad6 and its human homolog RNF20/RNF40-hRAD6A. *Mol. Cell* **83**, 3080-3094.e3014 (2023).
2. S. Diaz, L. Li, K. Wang, X. Liu, Expression and purification of functional recombinant CUL2•RBX1 from E. coli. *Sci. Rep.* **11**, 11224 (2021).
3. M. Pan *et al.*, Structural insights into Ubr1-mediated N-degron polyubiquitination. *Nature* **600**, 334-338 (2021).
4. J. Li *et al.*, Cullin-RING ligases employ geometrically optimized catalytic partners for substrate targeting. *Mol Cell* **84**, 1304-1320 e1316 (2024).
5. J. Liwocha *et al.*, Mechanism of millisecond Lys48-linked poly-ubiquitin chain formation by cullin-RING ligases. *Nat Struct Mol Biol* **31**, 378-389 (2024).
6. H. S. Ai *et al.*, Mechanism of nucleosomal H2A K13/15 monoubiquitination and adjacent dual monoubiquitination by RNF168. *Nat. Chem. Biol.*, (2024).
7. J. Lei, J. Frank, Automated acquisition of cryo-electron micrographs for single particle reconstruction on an FEI Tecnai electron microscope. *J. Struct. Biol.* **150**, 69-80 (2005).
8. J. Zivanov *et al.*, New tools for automated high-resolution cryo-EM structure determination in RELION-3. *eLife* **7**, e42166 (2018).
9. G. Kokic *et al.*, Structural basis for RNA polymerase II ubiquitylation and inactivation in transcription-coupled repair. *Nat. Struct. Mol. Biol.* **31**, (2024).
10. E. R. Watson *et al.*, Molecular glue CELMoD compounds are regulators of cereblon conformation. *Science* **378**, 549-553 (2022).
11. J. Jumper *et al.*, Highly accurate protein structure prediction with AlphaFold. *Nature* **596**, 583-589 (2021).
12. E. F. Pettersen *et al.*, UCSF chimera - A visualization system for exploratory research and analysis. *J. Comput. Chem.* **25**, 1605-1612 (2004).
13. P. Emsley, B. Lohkamp, W. G. Scott, K. Cowtan, Features and development of Coot. *Acta Crystallogr. D* **66**, 486-501 (2010).
14. P. D. Adams *et al.*, PHENIX: a comprehensive Python-based system for macromolecular structure solution. *Acta Crystallogr. D* **66**, 213-221 (2010).
15. E. S. Fischer *et al.*, Structure of the DDB1-CRBN E3 ubiquitin ligase in complex with thalidomide. *Nature* **512**, 49-53 (2014).

16. C. Heim, M. D. Hartmann, High-resolution structures of the bound effectors avadomide (CC-122) and iberdomide (CC-220) highlight advantages and limitations of the MsCI4 soaking system. *Acta Crystallographica Section D* **78**, 290-298 (2022).